In-Vivo X-Ray Fluorescence Assessment of Iron Levels in the Skin for β-Thalassemia Patients

In-Vivo X-Ray Fluorescence Assessment of Iron Levels in the Skin for β-Thalassemia Patients

By

Ibrahim Abu Atiya, B.Sc.

A Thesis

Submitted to the School of Graduate Studies

in Partial Fulfilment of the Requirements

for the Degree

Master of Science

McMaster University

MASTER OF SCIENCE (2012) McMaster University
(Medical Physics) Hamilton, Ontario

TITLE:	In-Vivo X-Ray Fluorescence Assessment of Iron Levels in the Skin for β-Thalassemia Patients
AUTHOR:	Ibrahim Abu Atiya, B.SC.
SUPERVISORS:	Dr. Michael J. Farquharson
	Dr. Fiona E. McNeill
NUMBER OF PAGES:	xi, 76

Abstract

The purpose of this study is to assess the feasibility of a non-invasive, reliable, and cheap method to evaluate iron-overload in beta-thalassemia major patients. The approach taken was through the possibility of in-vivo measurement of iron in the skin using a technique called x-ray fluorescence (XRF). It was hoped that the quantification of iron levels in the skin will correlate with those levels in major parenchymal organs, such as the liver and the heart – where most iron deposition occurs in thalassemic patients. Water phantoms were used to produce a calibration line with an R^2 value of 0.998. Skin, liver and heart tissues from 36 control mice were measured and their iron levels quantified. Iron concentration range in the skin was found to be -2 – 38 ppm with an average of 9.8 ± 1.6 ppm. Significant correlation was found between the iron levels in skin vs. heart (R_s^2 of 0.382); however, it was not significant in skin vs. liver (R_s^2 of 0.080). Skin biopsies from various sites of 6 cadavers were investigated in a synchrotron light source facility (CLS in Saskatoon, SK). Maps of iron, zinc and calcium distribution as a function of skin depth were then constructed. It was found that all three elements were significantly present in the epidermal layer compared to the dermal one. Calcium and zinc were present in the entire epidermis, whereas iron was mainly concentrated at the deepest region of the epidermis. It was also concluded that skin samples from the back, arm and thigh gave the clearest elemental distribution.

Acknowledgements

There are so many people I would like to thank for all their substantial support that kept me going to reach this point of my academic achievement. Foremost, I would like to express my sincere gratitude to both of my supervisors, Prof. Michael Farquharson and Prof. Fiona McNeill for their continuous support of my MSc thesis. They have been of a great guidance and a wealth of knowledge. I also would like to thank my other committee member, Dr. Nicholas Bock for his insightful comments and guidance.

A very special thank you goes to Elstan Desouza, who has been of a tremendous help. I want to thank him for his patience and motivation. His guidance helped me in all the time of this research. Alia Al-Ebraheem, Lesley Egden and Eric Da Silva have been of a great assistance in various parts of my MSc and their help is greatly appreciated. I also want to thank Jason Falladown and Scott McMaster for their help with the machine shop and their assistance around the laboratory.

The beautiful ladies at the medical physics office, Wendy Malarek, Nancy Brand, Fiona Ahlang and Linda Ellis were of great assistance with all the administration work that made my life much easier. Thank you very much!

To all my amazing colleagues, thank you a million for the wonderful two years I have spent with you. All the talks, the jokes, the pranks, and the dinners we had together will always be those especial moments that I will cherish forever. Especial thanks go to

Farshad, Peter, Xin, Yicheng, Kiara, Tuan, Ashley, Sahar, Jatin, Nataliya, Manuela, Phanisree, James H, Zahra, Jameel, Molhem, Olga, and James G. Wow! Big Family!

My sincere thank you also goes to all my uncles and aunts and to my siblings Nadera and Adnan for their support and enthusiasm. I want to thank my Grandparents Khitam and Adnan Sr. for believing in me.

Thank you… is not enough to express my appreciation to all the unconditional love and support I constantly received from my parents Mohamed and Mona. Thank you so much for always being there for me! Thank you for believing in me! Your love and support is what keeps me going in this life achieving my goals. This work is dedicated to you.

Table of Contents

List of Figures

List of Tables

Chapter 1: Introduction

1.1. Iron (Fe)

Iron is the 26th element in the periodic table. It is the fourth most abundant terrestrial element in the earth's crust (~ 4.7%). [1] Iron exists in a wide range of oxidation states: -2 to +8, which gives it the capability to donate and accept electrons. Ferrous (Fe^{2+}) and ferric (Fe^{3+}) are the two most common states. As a result, iron is a very important nutrient for most living organisms, as it has the capability to bind with many oxygen-binding molecules, such as hemoglobin.[2] However, excess iron will generate into reactive free-radical ions, which could be very damaging to cells and tissues.[2,3]

On average, the human body contains 3-5 g of iron, of which about 70% is used for hemoglobin synthesis. The basic outline of iron metabolism in the body is as follows: iron absorption from nutrients occurs in the duodenum region of the small intestine. In the intestinal lumen, Fe^{3+} is reduced to Fe^{2+}, which is then transported across the duodenal epithelium. The next step involves the reoxidation of Fe^{2+} back to Fe^{3+}, which is then attached to the plasma iron carrier: transferrin. Transferrin will then deliver the iron to the bone marrow and tissues for iron-containing protein production.[2,3] Excess intra cellular iron will be removed by a protein called ferritin[3] and stored in the liver.[2,3]

1.2. Thalassemia

Thalassemia (British English: Thalassaemia) is a hereditary autosomal recessive blood disorder originating from the Mediterranean region, thus the name comes from the Greek *thalassa* for sea and *-haima* for blood. [4-6]

Hereditary autosomal disorder means that the gene responsible for the disease is not found in the sex chromosome. Thalassemia has a recessive pattern of inheritance [5] (although dominant thalassemia has been reported [6]), which means that both parents have to be carriers in order for a child to be affected (figure 1.1).

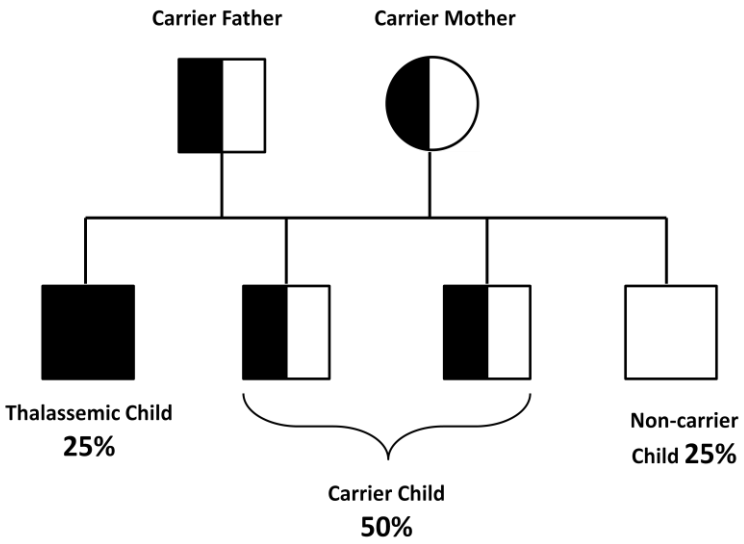

Figure 1.1: Thalassemia genetic inheritance

Hemoglobin is an iron-containing protein found in red blood cells. It consists of a heme ring and four globin chains: two alpha chains and two beta chains [4, 7] (figure 1.2). In healthy individuals, the production of alpha and beta chains is balanced.

Individuals with α-thalassemia have a deficiency in the production of alpha chains, whereas those with beta-thalassemia have a reduced production in the number of beta chains, or they are not produced at all. [4, 7, 8]

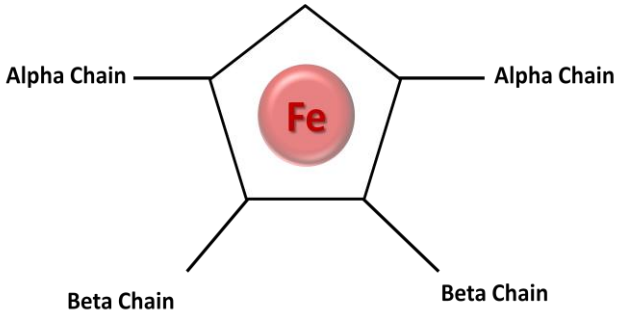

Figure 1.2: Hemoglobin basic structure

For the purpose of this study, the focus will be on β-thalassemia. β-thalassemia is "caused by any of more than 200 point mutations or, rarely, the deletion of both the beta-globin genes" in chromosome 11.[4,6-8]

Thalassemia is considered one of the most common hereditary anemias in the world. [5,8] The World Health Organization (WHO) estimates that 1.5% of the world's population might be carriers (heterogeneous) of β-thalassemia,[6,7] and 1 in every 100,000 people in the world are symptomatic (homogenous).[6] This disease prevails among the communities originating from the Mediterranean, the Middle East, South and Central Asia, as well as Southern China.[5,7]

There are three different types of β-thalassemia: minor, intermedia, and major. [5-8]

Individuals with β-thalassemia minor have only one β-globin gene with the thalassemia mutation. [8] Those individuals are only carriers of the disease and are asymptomatic with only mild or no anemia.[6,8] Individuals with β-thalassemia intermedia have two beta-globin genes with the thalassemia mutation, where at least one of them is mild.[8] Those individuals suffer from mild to moderate anemia and usually do not require blood transfusion, depending on the severity.[6,8]

Individuals with β-thalassemia major have both of their beta-globin genes carrying a severe thalassemia mutation. [7,8] Those individuals are usually diagnosed with the disease within the first two years after birth.[6] Such children will suffer from growth retardation, abdominal enlargement, irritability, pallor, jaundice, splenomegaly (expansion of bone marrow), among other symptoms, and thus will require life-long blood transfusions to grow normally and survive.[4,6,8]

One way of diagnosing β-thalassemia is with a blood test. Such a test will determine the size of red blood cells (RBC) as well as the hemoglobin they contain. Due to the reduced number of hemoglobin, individuals with β-thalassemia will have paler RBC's that, also, are different in shape compared to normal individuals.[5]

Thus far, the only definitive curative therapy for β-thalassemia major is a bone marrow transplant. [4,5] This treatment was developed in 1981[5] and has a success rate of 80-90% for children who are identified early with no viral hepatitis development or severe overload (i.e. before receiving any treatments) and have a human leukocyte antigen

(HLA) with identical stem-cell transplant from a related donor. Otherwise, the process is very risky with 25-30% morbidity and mortality rate. [7]

The most common treatment for β-thalassemia major is a life-long blood transfusion. [4-8] Blood transfusions are preformed to maintain a minimum hemoglobin level of 9.5 – 10.5 g/dL,[4,7,8] which is usually done every two to four weeks. [6] Transfused patients may develop a series of complications; iron overload being the most serious. [5, 6]

"Hepcidin is a small peptide that inhibits iron absorption in the small bowel". [8] Normally, hepcidin levels are increased when iron levels are elevated in the body. Studies showed that β-thalassemia patients have much lower levels of hepcidin. Iron deposition mainly occurs in vascular organs, such as the heart, liver and endocrine glands, causing tissue damage to these organs, and eventually, dysfunction and failure.[4,8] In fact, 71% of β-thalassemia major patients die due to cardiac complications.[4,6]

The human body does not have effective ways to remove excess iron. As a result, iron-binders (chelators) are needed for excess iron excretion through the urine and/or faeces.[5,6] Chelation therapy usually starts after the patient has had 10–20 transfusions or when ferritin levels are above 1000 ng/ml.[6] One of the most used iron-chelator agents is deferoxamine (DFO).[4,6-8] The problem with DFO is that it is not orally absorbed; 8 to 12 hour of parenteral infusion for 5 – 7 nights a week is required. Thus, DFO is considered to be a painful process to the patient, as well as being costly and having other side-effects.[6] As a result, many chelator agents have been developed in

recent years, namely: deferiprone (DFP) and deferasirox. DFP is an orally active iron-chelator agent and has shown to be more effective in the removal of iron with much fewer side-effects. [4, 6, 7]

In order to ensure the effectiveness of chelation therapy (the need and the timing of treatment), assessment of iron-levels is crucial. There are many methods used to evaluate iron levels. "Serum Ferritin has in general been found to correlate with body iron stores".[6] However, this is considered unreliable, especially if the patient suffers from liver disease,[6,7] inflammatory disorders, and malignancy.[6] Another method is liver biopsy, which is considered the gold standard for accurate measurement of iron levels.[6,7] The down side of this method is that it is invasive and has a mortality rate of 0.1%.[9] A non-invasive option for iron-overload assessment is magnetic bio-susceptometry (SQUID), which is considered either equivalent or more accurate than liver biopsy; however, this technique is only available in four centres worldwide.[6,8] In recent years, many studies have shown that magnetic resonance imaging is a promising method to be used in iron overload assessment. This approach is still under-studied and needs long term research to approve its effectiveness. [6, 8]

When proper treatment of β-thalassemia major is achieved, those individuals usually live beyond 40 years of age. [6]

1.3. X-Ray Fluorescence (XRF)

XRF is a physical phenomenon that results in the emission of characteristic x-rays due to photon interaction with an atom in a process called the "photoelectric effect". This method is utilized in many scientific studies, such as in-vivo elemental analysis, chemical analysis and archeology.

The first step to achieve XRF is to have an initial photon beam source. This is provided either by the emission of gamma rays from a radioactive material, or by the emission of photons from an x-ray tube. When interacting with a target atom, a photon will be completely absorbed as its energy transfers to an inner-shell electron. The minimum energy a photon requires to remove an electron from an atomic shell, called the "absorption edge", has to be greater than or equal to the binding energy of the electron. This process will result in a vacancy in the inner shell of the atom, and thus, it becomes excited. An excited atom will always get back to its ground state; hence, an electron from an outer shell (higher energy shell) will transfer to the vacated space to be filled. As a result of the difference between the binding energies of the two shells, the excess energy will either be released as a characteristic (of the element) x-ray, or in a form of Auger electrons.[10-12] The probability for an atom in an excited state to emit an x-ray photon, in its first transition, rather than an Auger electron is called the "fluorescence yield", which increases as the atomic number, Z, increases.[11] The fluorescence yield for iron is 35.5%.[13]

Another concept that has to be explained is the different shells of an atom. Electrons orbit the nucleus in shells. These shells are identified by the letters K, L, M, etc. [12] with K being the innermost shell to the nucleus. Fluorescence from both K and L shells is possible, however, energies released due to L-shell vacancies are considered very small (0.7050 keV and 0.7185 keV [14]) in the case of iron to be detectable. On the other hand, energies released due to K-shell vacancies are much larger (Table 1.1) and they dominate the detectable photons. When a K-shell vacancy is filled by an L-shell electron, a K_α x-ray is produced (figure 1.3), whereas when it is filled by an M-shell electron, a K_β x-ray is produced. [12] Although the K_β has the larger energy of the two (since the energy difference between the K-shell and M-shell is larger), the K_α has a higher intensity, thus the K_α energy-line is the main focus of this study.

X-Ray Line	Energy [keV]	Relative Intensity
Kα1	6.3908	50
Kα2	6.4038	100
Kβ1	7.0580	17

Table 1.1: K-shell Characteristic x-rays produced from the fluorescence of iron [14]

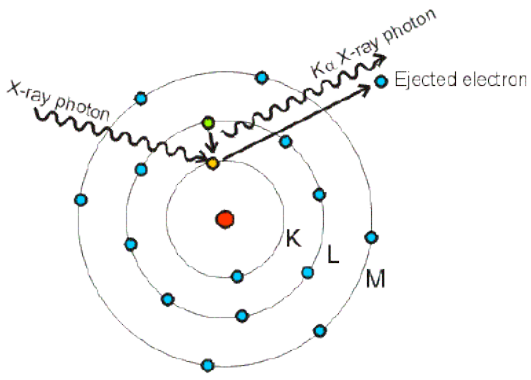

Figure 1.3: Kα x-ray photon production [15]

From Table 1.1, $K\alpha_1$ and $K\alpha_2$ are very close in value, and are indistinguishable when detected. Thus they are treated as one signal at 6.40 keV. It is also worth mentioning that incident beam energies just above the absorption edge will result in a maximum generated signal per incident flux. The K-absorption edge for iron is 7.11 keV. [14]

To know how deep in a sample iron atoms can be detected with XRF, the mean free path (MFP) from iron fluorescence has to be determined. MFP is the average distance traveled by a photon between collisions in a material. MFP depends on both the energy of the photon and the material of the sample. It is defined as: MFP = μ^{-1}, where μ is the linear attenuation coefficient. In water and soft tissues, the MFP for a 6.40 keV photon is 0.46 mm. This means that in water and soft tissue samples, a thickness of 0.46 mm will cause the attenuation of 37% (1/e) of the Kα Fe fluorescence.

In addition to photoelectric effect, scatter is another important photon interaction that is detected when using XRF techniques. There are two types of scattering interaction involved: elastic scattering (known as coherent) and inelastic scattering (known as Compton). In Compton scattering (for low energy x-rays), a collision between the photon and a free electron or a loosely bound one from the atom will occur. As a result of this collision, some of the photon energy will be transferred to the recoil electron, and the photon will change its direction. The new energy, E', of the photon is represented by: [10-12]

$$E' = \frac{E}{1 + {}^{E}/_{m_0 c^2}(1 - cos\theta)} \qquad (1.1)$$

where E is the initial energy, m_0c^2 is the rest mass energy of an electron, and θ is the angle between the initial and the scattered photon.

The energy produced by Compton scatter is not exactly at the expected energy (from eq. 1.1), but rather, it is distributed around it. This is called the Doppler broadening. The probability that a photon will be scattered into a solid angle dΩ is described by the differential Klein-Nishina collision cross section: [11, 12]

$$\frac{d\sigma_{KN}(\theta)}{d\Omega} = \frac{r_e^2}{2}[1 + k(1 - cos\theta)]^{-2} \times \left[1 + cos^2\theta + \frac{k^2(1-cos\theta)^2}{1+k(1-cos\theta)}\right] \qquad (1.2)$$

where r_e is the radius of the electron and k is the energy of the photon.

In coherent scattering, the photon interacts with the atom as a whole instead of a single electron. As a result of a relatively heavy atomic mass, the photon only changes its direction with no loss of energy.

1.4. Skin

Skin is the body's largest organ and covers its entire external surface. It contributes approximately 15% of the total body mass. [16] The skin is a very important organ because it provides the body protection from external environmental harm and from microorganisms; it regulates the body temperature through sweating; as well as being the location of vitamin D production. [17]

The skin consists of two layers; the outer epidermis layer and the inner dermis layer (figure 1.4: a). The junction between the two layers is not flat, but rather a cone-like surface.

The epidermis is an avascular (not supplied by blood) layer and receives its nutrients from the dermis via diffusion. The epidermis consists of five different layers (figure 1.4: b). The stratum basale is the deepest layer of the epidermis; just above the basement membrane (separating from the dermis). This layer is composed of a single layer of columnar to cuboidal-shaped cells. They are mitotically active. The newly formed cells push the older ones up towards the surface. Just above this layer is the stratum spinosum. This is the thickest layer in the epidermis (other than thick skin). It consists of four to six rows of cells, which are polyhedral in shape. This layer is created as a result of the cell movement from the basale layer. Cells at the bottom of this layer are still mitotically active; however, these cells stop dividing and get flattened as they move further up. The next layer is the stratum granulosum. This layer is three to five cell rows thick. The cytoplasm of the cells in this layer contain organelles called lamellar granules, which are formed by lipid bilayers. Those granules are discharged into the extracellular space and will act as a barrier that prevents aqueous liquid movement from or into the dermis. The next layer is the stratum lucidum. This layer is only present in thick skin (palm and foot). It is tightly packed with dead, flattened cells with no nuclei or organelles; however, it contains densely packed keratin filaments. This layer is very thin and it is barely visible. Lastly is the stratum corneum. It is the topmost layer of skin and the thickest layer of the epidermis

in thick skin. This layer mainly consists of flattened dead cells with no nuclei or organelles. [16, 17]

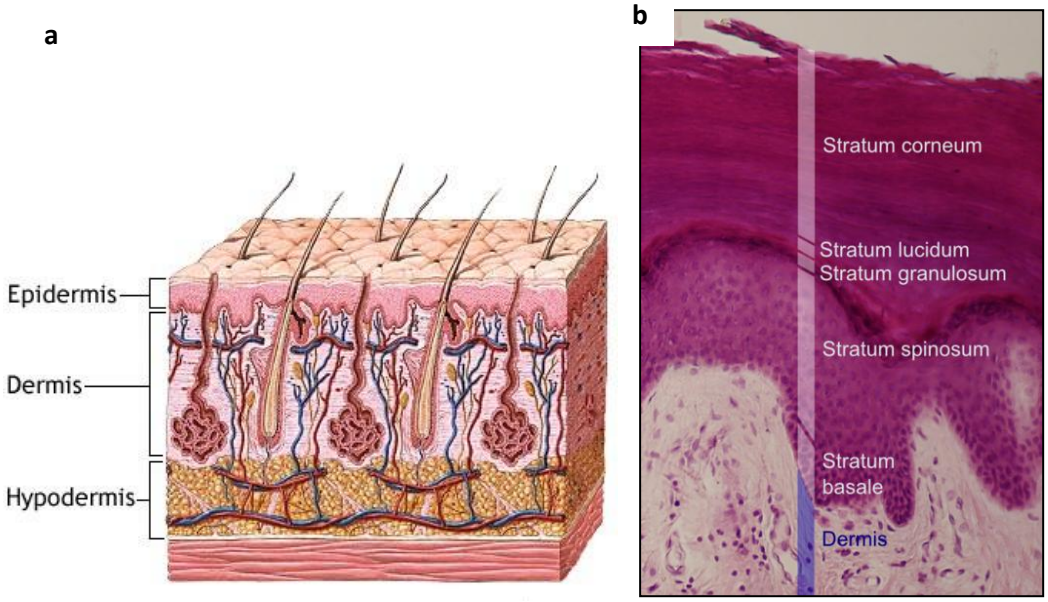

Figure 1.4: a: A diagram of the human skin. [18] **b:** A histologic image showing the different layers of the epidermis in thick skin.[19]

The dermis is the connective tissue layer of the skin and is thicker than the epidermis (table 1.2). It consists only of two layers. The top one is the dermal papillae, which is mainly filled with connective tissue fibers, fibroblasts, blood vessels, capillaries, and other loose connective tissues. Under this layer comes the deepest layer of the skin: the reticular layer. This layer is thicker than the dermal papillae. It also contains connective tissue fibers but fewer cells than the dermal papillae. [17] This layer contains sweat glands and their ducts, sebaceous glands, hair follicles, arrector pili muscles, and mechanoreceptors. [16] There is no clear boundary between the two layers of the dermis.

Below the dermis layer, there is another layer called hypodermis (aka subcutaneous fat). Hypodermis is not considered part of the skin and it is the site of fat storage.

	Male		Female	
Site	**Epidermis (μm)**	**Dermis (μm)**	**Epidermis (μm)**	**Dermis (μm)**
Thigh (medial)	**50-70**	**1100-1300**	**18-55**	**830-1000**
Thigh (lateral)	**39-78**	**1200-1800**	**45-63**	**950-1400**
Upper arm (medial)	**37-52**	**1200-1300**	**34-43**	**730-800**
Upper arm (lateral)	**41-71**	**1300-1900**	**40-45**	**670-1300**
Back	**49-92**	**2200-2500**	**45-61**	**1500-1900**
Sole	**940-1400**	**1300-1800**	**850-1100**	**1500**

Table 1.2: Example of epidermis and dermis thicknesses from various parts of human skin [20]

The skin is considered a very suitable tissue for this study because it is readily accessible for examination and easy to be used as a non-invasive target for XRF experimental purposes.

1.5. In-Vivo XRF Measurements of Iron in Skin: Previous Studies

The importance of many metallic elements in the function of the human was recognized long ago. These elements are present in very small amounts (trace) and were very hard to quantify due to the lack of suitable technologies. Many analytical techniques were developed and it is now possible to measure these elements. One of these techniques is x-ray fluorescence. [21] XRF has been used as a technique for measuring various trace elements in-vivo since the early 1970s. [12] However, there are

only a few studies that have been preformed for in-vivo iron measurements in the skin. The most extensive work on iron levels in the skin in β-thalassemia patients has been reported by Gorodetsky and Farquharson.[9, 22-26] Gorodetsky *et al.*[22] used XRF to measure iron levels in two locations of the skin (skin from the thenar eminence and skin from the flexor surface of the forearm) in normal controls, β-thalassemia intermedia and β-thalassemia major patients. Table 1.3 summarizes their findings.

	β-Thalassemia Inter.		**β-Thalassemia Major**		**Normal Controls**	
	Mean ± SD	**Range**	**Mean ± SD**	**Range**	**Mean ± SD**	**Range**
Fe-T	16.8 ± 11.4	6.7-58.3	35.1 ± 18.3	13.1-120.0	11.5 ± 2.4	5.9-14.0
Fe-A	17.7 ± 10.6	7.1-40.4	46.5 ± 24.9	14.4-150.0	10.2 ± 2.5	6.0-14.4

Table 1.3: Summary of Gorodetsky *et al.* [22] findings of iron concentrations in normal controls and β-thalassemia patients. T = Skin of thenar eminence (palm); A = skin of the flexor surface of the forearm. Values measured in parts per million.

In one study, Farquharson *et al.* [25] used iron-loaded rats (Sprague-Dawley rats) to compare iron levels in skin to those in liver, heart and spleen. They found the R^2 values for the liver, heart and spleen to be 0.86, 0.86 and 0.88 respectively. They concluded that there is a strong correlation between these organs and that XRF can be used as a non-invasive method for iron assessment in β-thalassemic patients.

Another study showing iron measurements in the skin using XRF was done by Ackerman *et al.* [27] The research was done on varicose ulcers rather than β-thalassemia. They found the mean concentration of iron in normal skin to be 14 ± 2.5 ppm, which is similar to Gorodetsky's results, and a range of 3 – 46 ppm, which is a much wider range compared to Gorodetsky's.

In a more recent study, Marcelo *et al.* [28] used a portable XRF system to measure iron concentration in the skin of healthy individuals and β-thalassemic patients. They reported that thalassemia patients showed 74 ± 6 ppm of iron compared to 53 ± 5 ppm in healthy volunteers.

In addition to XRF, other techniques were used to assess iron levels in various organs. In their SQUID biosusceptometer study, Pakbaz *et al.* [29] measured liver iron concentrations in 160 thalassemia and sickle cell patients and compared them to healthy individuals. The iron concentration range was 1000 – 2100 ppm (wet weight) in the iron-load patients compared to 90 – 340 ppm for healthy individuals. Using neutron activation analysis (NAA) technique, Molin *et al.* [30] found the average iron concentration in normal human skin to be 28.8 ± 9.9 ppm. This study was performed on dry weight samples, however. In another NAA study, Parr *et al.* [31] collected autopsies from healthy individuals who died suddenly as the result of accidents. They found the average iron concentration in the liver (6 samples) to be 183 ± 86 ppm and a range of 42 – 252 ppm.

In this study, iron concentrations in the skin, liver and heart samples of control mice (strain: triple transgenic for Alzheimer's disease (3XTg-AD)) were examined. No previous literature work was found, measuring iron concentrations in these desired organs, for this particular mouse strain. Most researches performed on 3XTg-AD were Alzheimer's disease related studies. Besides the XRF iron measurement in rats discussed above (Farquharson *et al.* [25]), many other studies were done on other

rodents with different techniques. However, most of those studies used dry weight organs instead of the wet weight ones. The results from these two different measurements cannot be directly compared since dry weight measurements will give a much higher iron concentration compared to the wet weight (higher µg Fe per g of tissue). Few studies dealing with wet weight tissues were found. One of those studies was Milstone *et al.* [32], where they used the bathophenanthroline method described by Torrance and Bothwell [33], to measure non-heme iron in tissues. They found 12 control (non-transgenic) mice to have average iron concentrations of 376 ± 18.5 ppm, 48.2 ± 0.5 ppm and 15.4 ± 1.7 ppm in liver, heart and ear epidermis samples, respectively. In another study, using the same method, Whittaker *et al.* [34] examined the iron concentrations in the livers and hearts of 11 control Sprague-Dawley rats. The outcome of their study was an average of 112 ± 5 ppm of iron in the liver and 34.4 ± 7 ppm in the heart.

Chapter 2: Experimental Setup

2.1. The XRF System

The XRF system [11] used in this study has a molybdenum-target x-ray tube; model XTF5011, from Oxford instruments (Scotts Valley, CA). The tube's maximum anode voltage is 50 kV and its maximum anode current is 1 mA. It has a Be window with thickness of 0.005". The tube is encased in a brass shielding to prevent radiation from leaking anywhere but the beam port.

The geometry that was chosen for this system was a 90° source-to-detector angle, with the sample being at 45° relative to both. The reason for this choice was due to the lower minimum detection limit (MDL) achieved when using a 90° geometry. In a previous study preformed on arsenic using this system showed that the MDL was 3.5 ± 0.2 ppm with the 90° geometry, whereas, it was 10.3 ± 0.5 ppm for the 180° geometry. [11]

The system was built in a box of two chambers; one where the sample is placed with the beam source and detector, and the other being the control area where the x-ray tube is placed. The box is made of Lucite (also known as Plexiglass) with wall thickness of 1.8 cm and dimensions of 70 cm x 50 cm x 27 cm. To ensure no radiation leakage, the

first chamber was shielded from the outside with 3 mm thick copper plates to the top and sides, 1.5 mm thick copper plates to the bottom, and extra 1.5 mm copper plates at the corners on the inside. In addition to that, and to ensure safety according to health physics regulations, a 12 mm thick copper shutter was installed at the opening of the x-ray tube, as well as interlocks at the doors that open into the sample chamber, to eliminate accidental exposure while the system is in operation.

A 313 mm aluminum tube was used to direct the beam towards the sample. A 20 mm thick aluminum collimator, with a 5 mm diameter hole, was used to control the size of the beam. A plastic ring was used to hold the tube and collimator together. Since the sample is held at 45° angle (relative to the x-ray tube) the beam hits the sample with an ellipse shape (rather than circular) with 5.3 mm vertical and 7.5 mm horizontal dimensions. The sample is positioned at a distance of 17 mm from the collimator and 28 mm from the detector (figure 2.1).

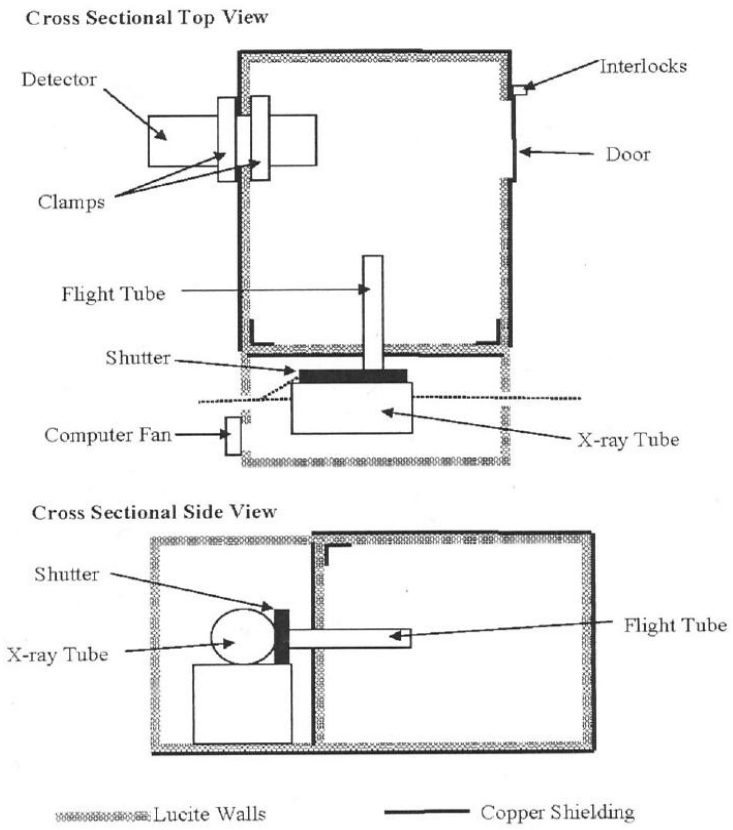

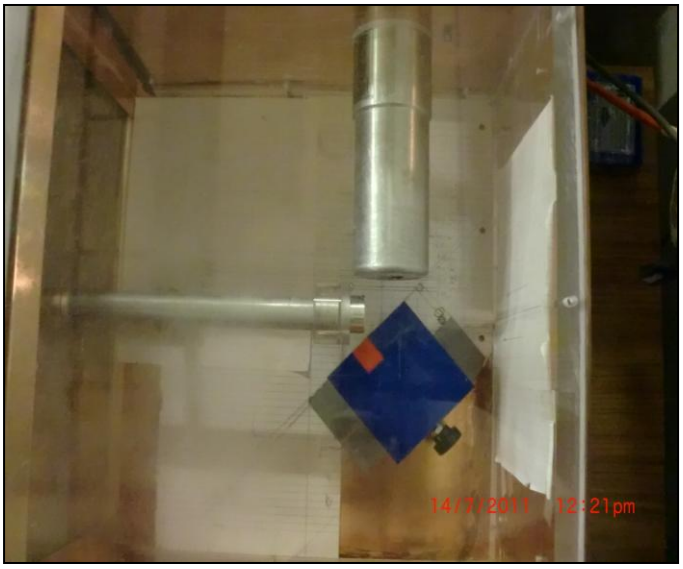

Figure 2.1: a: Top and side views of the XRF system. [11] **b:** Picture of the top view of the system. The length of the x-ray tube plus the collimator is 337 mm

2.2. Detector and Signal Processing

An ORTEC silicon lithium drifted (Si(Li)) detector (SLP-10180P) was used in this study. The detector crystal has an active diameter of 10 mm and sensitive thickness of 5 mm. Its beryllium window has a thickness of 25 μm. The detector's resolution at 5.9 keV is 180 eV.

For signal processing, DSPEC Plus™ (Digital Spectrometer) with its associated software, Maestro™ was used. The DSPEC Plus™ allows the flexibility to choose the desired rise time, gain, and real or live times. Maestro™ plots the outcome spectra as Counts vs. Channel# and allows choosing multiple regions of interest (ROI). It also provides important information for data analysis, such as the gross and net areas for the selected ROI, the resolution of peaks (full width half maximum), and the system's dead time.

2.3. Filtration

A very important concept to consider when producing x-ray photons is a filter. The main purpose for using a filter is to eliminate unwanted photons as well as reducing dead time. [11] When the system was tested without a filter, it had a dead time of more than 80% compared to 14% when a 100 μm molybdenum (Mo) filter was used for the exact experimental setup. Also, the usage of a Mo filter resulted in the absorption of Bremsstrahlung radiation and sparing the scatter peaks of both the Kα and Kβ of the Mo XRF (figure 2.2).

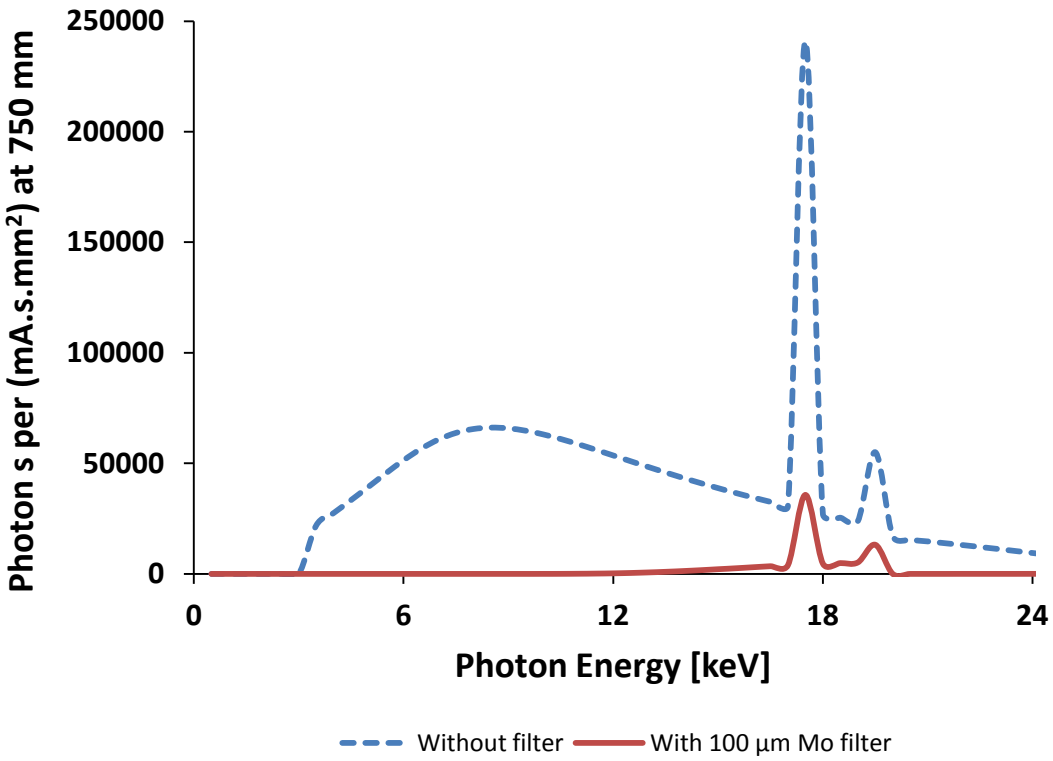

Figure 2.2: The spectrum of Mo-target x-ray tube without a filter is compared to the spectrum of the same tube with a 100 µm Mo filter. Software called *Report 78: Catalogue of Spectral Data of Diagnostic X Rays and other Data* (IPEM. York, UK. 1997) is used to generate these spectra

Figure 2.2 shows a significantly elevated background for the region between 3 keV and 17 keV, when no filter is being used. This elevation will cause the disruption of the iron peaks at 6.40 keV (very low signal-to-noise ratio), thus the iron presence in a material will be impossible to measure. On the other hand, the usage of a 100 µm Mo filter has resulted in a flatter background for the same region after eliminating the Bremsstrahlung radiation. The measurement of iron peaks is now possible.

Chapter 3: Calibration Line

3.1. Phantom Holders

Since the focus of this study is to measure iron, an appropriate material to be used as phantom holder was investigated. Various materials were placed in front of the beam to be tested. Pieces of nylon, resin, a Petri dish, and plastic were measured, as well as the system background (no target materials present).

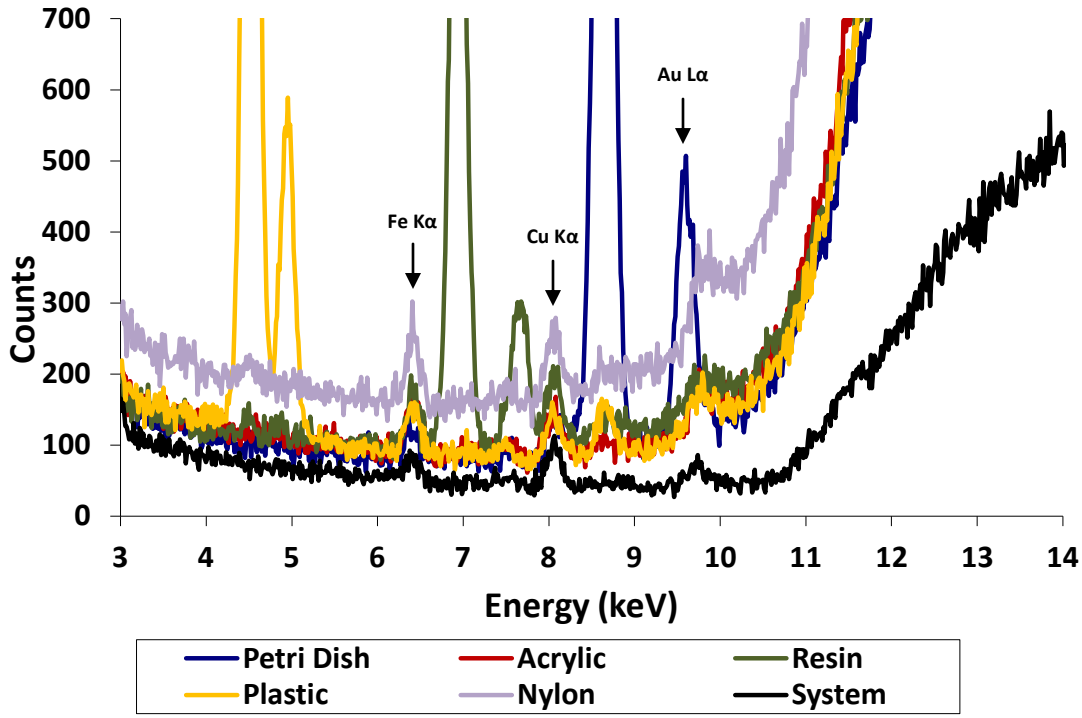

Figure 3.1: Maestro spectra of various materials tested to be used as phantom holders. X-ray tube settings were 23.7 kV for the voltage and 0.3 mA for the current. Each sample was run for a live time of 1000 seconds.

From figure 3.1, it is clear that there is a small presence of iron (at Kα of 6.4 keV) in the system. It was also noticed that the tested materials have similar iron peak sizes, but slightly elevated background (especially nylon) compared to the system due to the scattering of photons off the testing blocks. All measurements also showed the presence of copper (at Kα of 8.03 keV) – because of the copper shielding of the system – as well as gold (at Lα of 9.7 keV) – which is present in the detector itself. Some materials have also shown the presence of other elements, such as cobalt (at Kα of 6.9 keV (which is very close to the Kα of iron) and Kβ of 7.6 keV) in resin, zinc (at Kα of 8.6 keV and Kβ of 9.6 keV) in Petri dish, titanium (at Kα of 4.5 keV and Kβ of 4.9 keV) and small amount of zinc in plastic. Ideally, a phantom holder material should not contain any unnecessary elements to achieve a clean background and to avoid interference with the studied element of interest. This is also very important because with a clean background, it would be easy to identify the presence of any other elements in the studied tissues (i.e. skin, liver, and heart).

Another material that was considered was high density polyethylene (HDPE). HDPE is the material that is being used by Dr. Farquharson`s lab group as a phantom holder and was proven to be appropriate for XRF research. Blocks of HDPE (5 cm x 5 cm x 1cm) were purchased from P&A Plastic Inc. (Hamilton, ON).

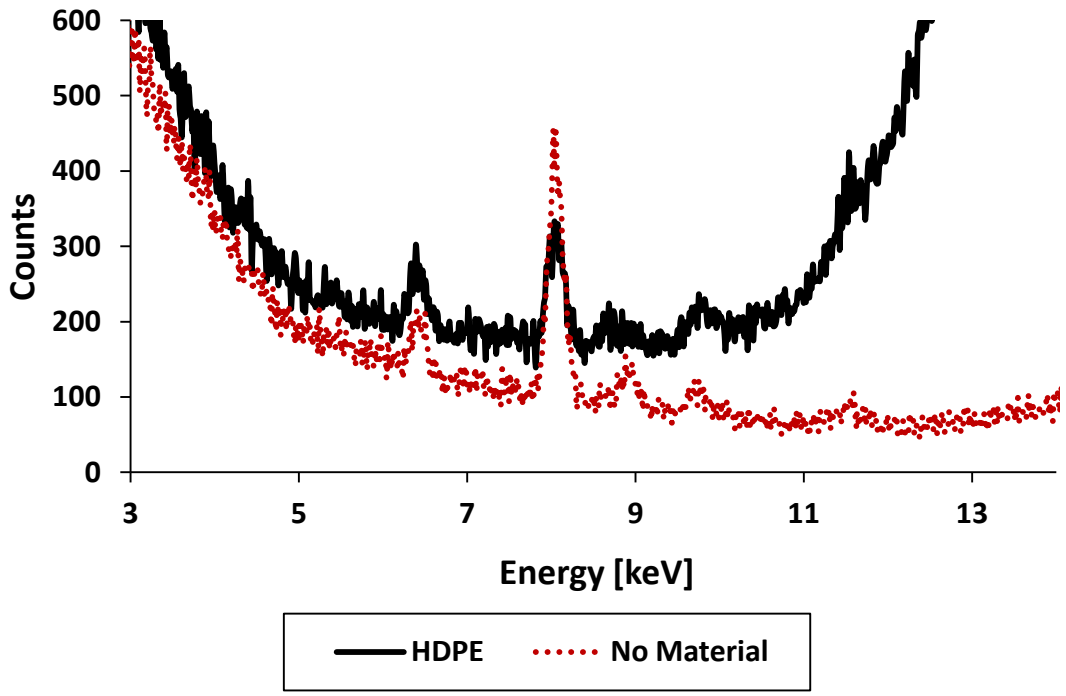

Figure 3.2: Maestro spectra of the system background (no materials used) and HDPE as a target. X-ray tube settings were 37.5 kV for the voltage and 0.6 mA for the current. Each sample was run for a live time of 1200 seconds.

Figure 3.2 compares the spectrum of HDPE with the system background. The main focus here is what elements are present and how their peaks compare, rather than the shape of the background (the backgrounds will behave differently due to the different media of scattering radiation). Both spectra show the exact number of elements present, which means that HDPE does not contain any element that is not already present in the system. Both spectra contain iron (6.40 keV), copper (8.03 keV and 8.91 keV) and gold (9.71 keV and 11.58 keV). Both iron peaks are similar in size, while the copper peak from the system is much larger. This is because the copper shielding is the main reflector of photons (compared to the HDPE block). As a result of figure 3.2, HDPE was chosen as an appropriate material to be used as a phantom holder. Figure

3.3 shows a typical spectrum produced when an HDPE block is placed at a 45° angle between the beam source and the detector.

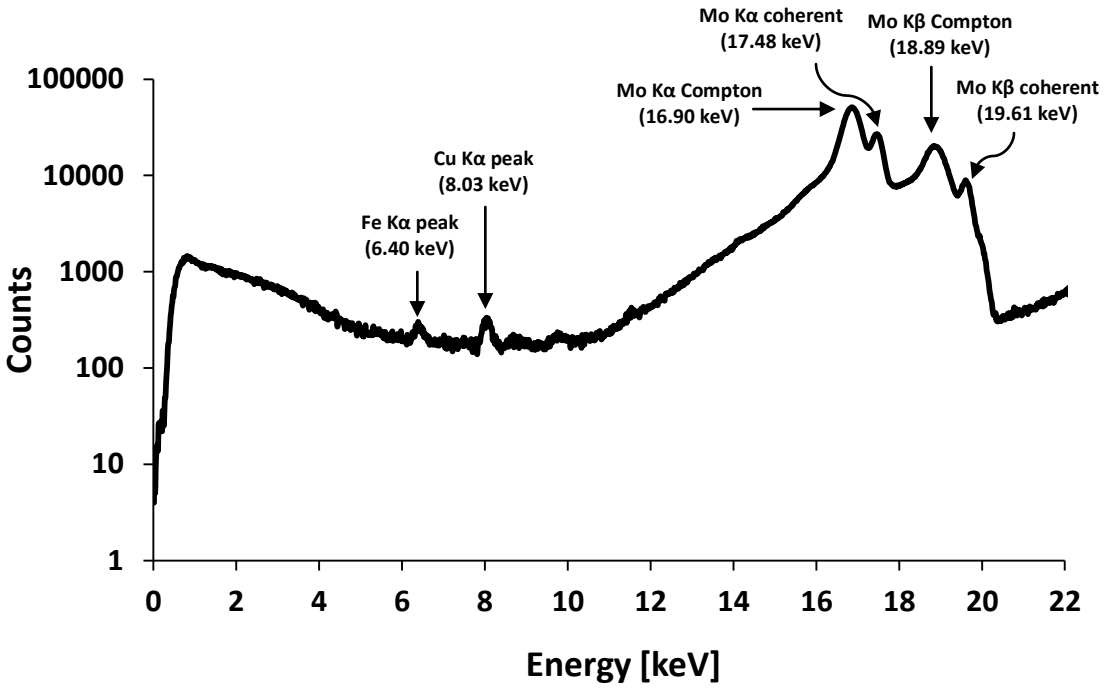

Figure 3.3: HDPE spectrum in Maestro. Logarithm scale was used for y-axis.

3.2. Phantoms

The purpose for phantoms is to create a guideline to quantify the concentration of an element in a measured object. The phantom has to mimic that object as much as possible in terms of density, composition and geometry.

In this study, soft tissues (i.e. skin, liver, and heart) will be measured. Knowing that the major component that makes up soft tissues is water, using water phantoms is

ideal. Both water and soft tissues have a density of 1000 kg/m^3. The only issue with using water is leakage, since the phantoms have to be held vertically.

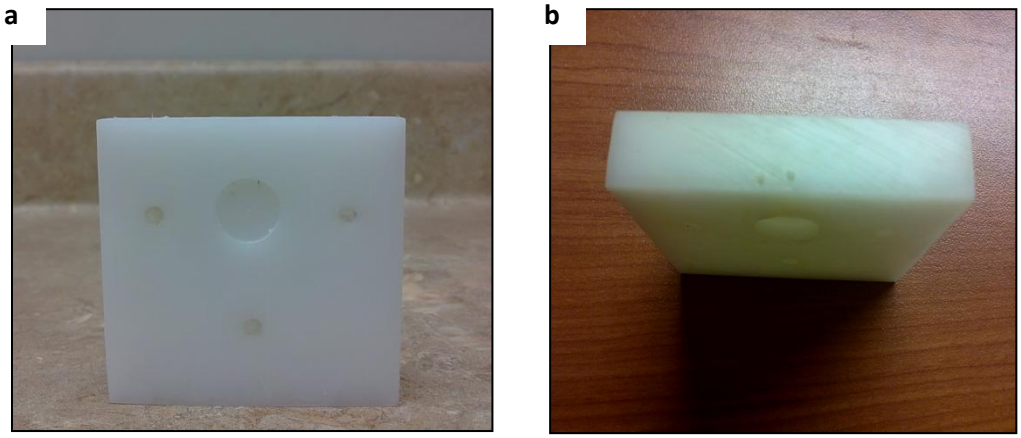

Figure 3.4: a: A side view of the phantom holder, with a hole of 1.1 cm in diameter and 2 mm in depth. **b:** Top view of the phantom holder showing the two holes leading to the bigger, side hole.

The solution was to design the phantom holders in a way that allowed water to be held vertically without leakage. A 1.1 cm diameter hole was drilled in the middle of the surface of the HDPE block (figure 3.4 a.). This hole was 2 mm in depth with a flat bottom. Silicon paste P4 (Wacker Chemie AG, Munich, Germany) was applied to the surface around the hole and a 4 μm thick 3525 ULTRALENE XRF film (SPEX SamplePrep LLC, Metuchen, NJ) was placed on top of that surface to tightly seal the hole. To fill the hole with the phantom solutions, two holes on top of the phantom holder were drilled (figure 3.4 b.). One hole was used to inject the solution using a needle and a syringe. The purpose of the other hole was to let air out while the solution was injected into phantom holder.

3.3. Iron solution

After choosing water to be used as phantoms and machining the holder accordingly, preparing iron solutions with different concentrations was investigated. The iron solution (Ultra Scientific Analytical Solutions, USA) used was composed of water with diluted nitric acid (2% HNO_3). Every 1 gram of solution had 1000 µg of iron, giving an iron concentration of 1000 parts per million (ppm). To produce different concentrations of iron phantoms, the iron solution had to be diluted with deionised water according to the desired ppm (table 3.1)

ppm	Iron solution [g]	Added water [g]
0	0	1
10	0.01	0.99
50	0.05	0.95
75	0.075	0.925
100	0.1	0.90
500	0.5	0.5
750	0.75	0.25
1000	1	0

Table 3.1: Examples of producing 1 gram of iron solutions with different concentrations

3.4. Voltage & Current

The next step was to confirm the behaviour of the signal intensity (energy flux density) as a function of the x-ray tube's voltage and current. In theory, the intensity of x-ray radiation is directly proportional to the applied current and to the square of the voltage. [35]

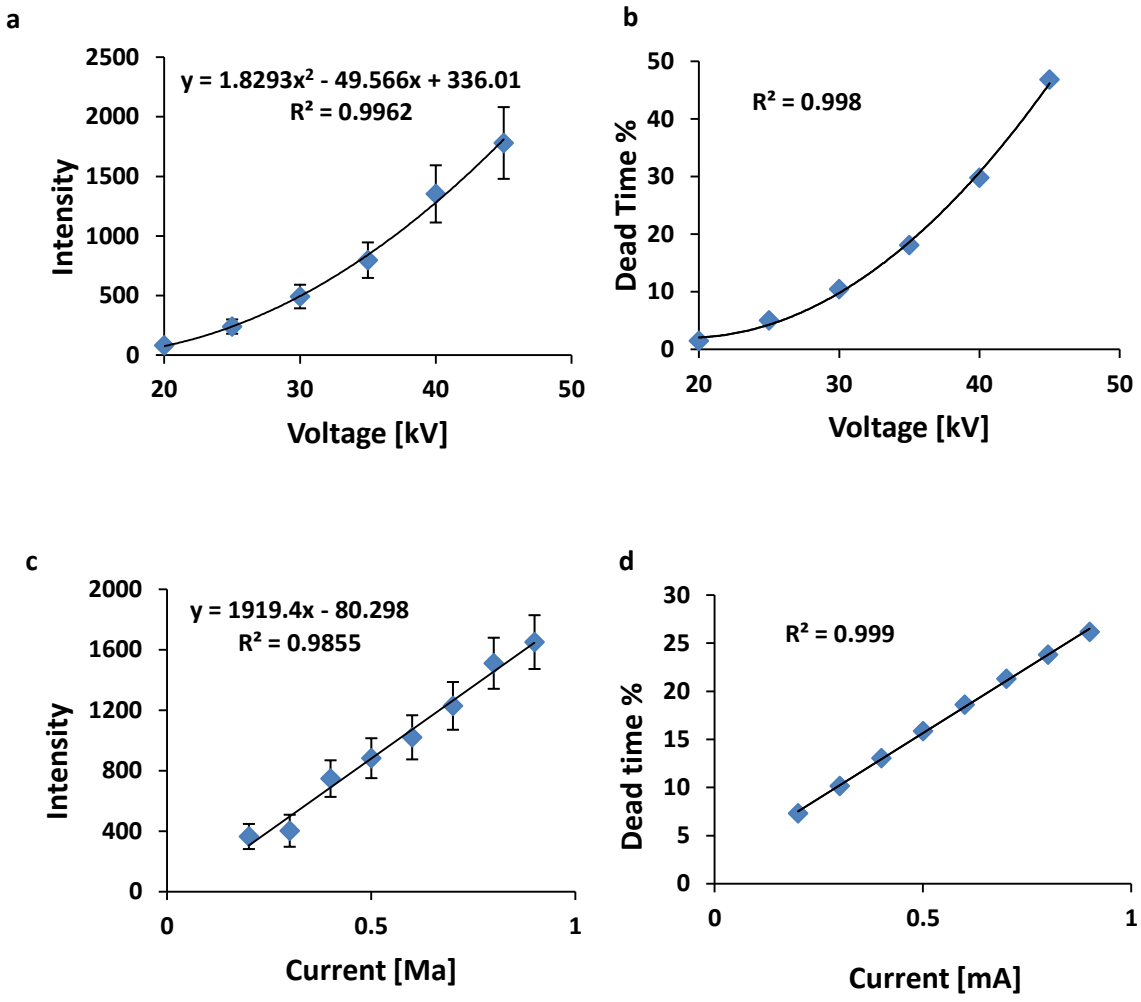

Figure 3.5: a: shows signal intensity as a function of voltage, while **b:** shows the corresponding dead time. The current was kept constant at 0.6 mA. **c:** shows signal intensity as a function of current, while **d:** shows the corresponding dead time. The voltage was kept constant at 35 kV

As seen in figure 3.5, both the current and voltage confirm the theoretical behaviour as stated above. The signal intensity has a second order polynomial relationship with the voltage and a linear relationship with the current.

Ideally, maximum voltage and current would be chosen to obtain maximum signal intensity; however, the trade-off would be a very high dead time. As a result, the voltage and current were chosen according to the desired dead time. At the beginning of this research, 37.5 kV voltage and 0.6 mA current were chosen to obtain ~ 20% dead time (later on ~ 10% was chosen).

3.5. Iron Concentration Calibration Graph

Water phantoms with various iron concentrations were prepared. Since the focus of this study is on lower concentrations, 0, 10, 20, 40, and 60 ppm were chosen. Each prepared sampled was measured with XRF three times for statistical reasons. Peak analysis was performed using PeakFit version 4 (Systat Software Inc.). All peak areas in this study were normalized to time (further discussion is shown in chapter 5)

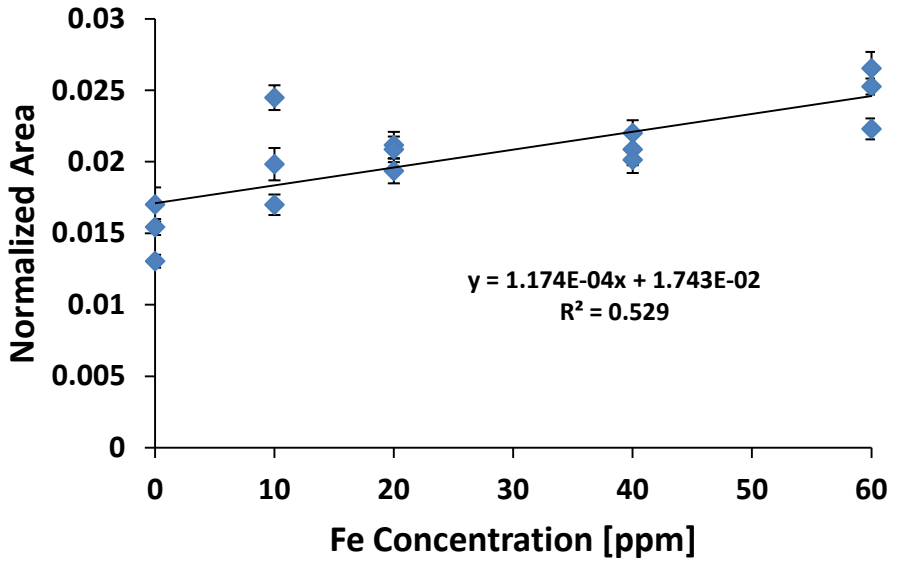

Figure 3.6: Calibration graph of normalized iron peak areas as a function of iron concentration. Each measurement was done for 1200 seconds live time. The voltage was 37.5 kV and the current was 0.6 mA.

Theoretically, iron signal intensity should be linearly proportional to the iron concentration. However, as seen in figure 3.6, this was not achieved. The R^2 of the linear fitting was 0.529. This result indicated that something was not correct and further investigation was necessary.

3.6. Testing the Effect of Rise Time

One of the pulse characters that might be affecting the signal intensity is full width half maximum (FWHM). FWHM is the measurement of the pulse's width at its half amplitude. FWHM is a direct indication of the pulse's resolution; the narrower the FWHM the better the resolution.

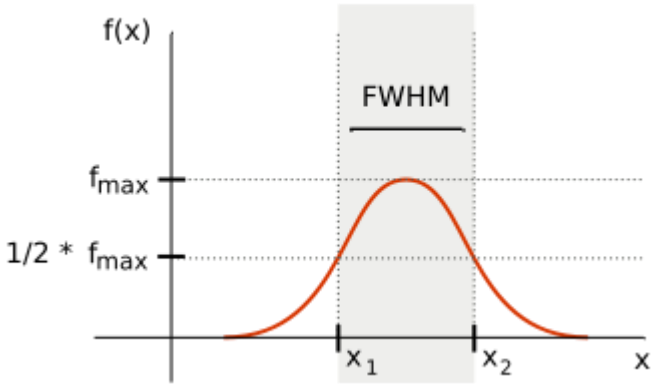

Figure 3.7: Full Width Half Maximum [36]

One of the parameters affecting FWHM is the pulse's rise time. Rise time is generally defined as the time needed for a pulse to rise from 10% to 90% of its maximum amplitude. [10] The pulse processing instrument used (DSPEC Plus™) allows for rise

time to be selected as desired. The optimum rise time is the lowest value that will result in the lowest FWHM (figure 3.7). [37]

The next experiment was performed to test the effect of rise time on the signal resolution. In this experiment, a block of steel was used to obtain high counts for good statistics in a short time.

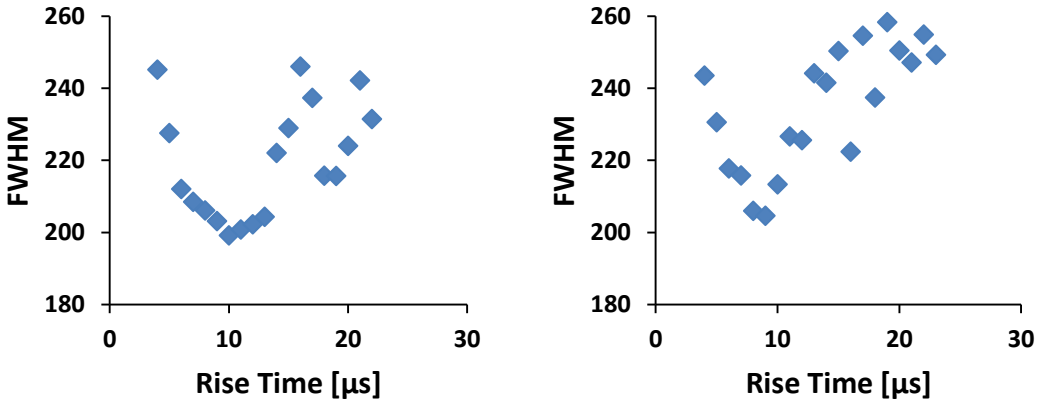

Figure 3.8: FWHM as a function of rise time. Two trials were conducted. Each measurement was done for 60 seconds live time. The voltage was 37.5 kV and the current was 0.6 mA.

From figure 3.8, it can be seen that there is not a clear trend for the FWHM behaviour as a function of rise time. Also, for two identical trials, the data was not reproducible.

While a third trial was being preformed, an electric saw was used in the same room where the experiment was taking place. A sudden signal broadening was observed as the saw was used. The effect of using power machines was investigated next.

3.7. The Effect of Power Machine Usage on Signal Quality

The Tandem Accelerator Building of McMaster University (where this study was done) has three accelerators, experimental instruments, and heavy machine shops that are being used intensively on a daily basis. The influence of these instruments has various effects on the quality of data collection of this study, depending on the instrument that is being used and how close it is to the XRF system.

The experiment outline to measure the effect of power machines was as follows: a heavy-duty grinder (8000 rpm motor) was used to test its effect on the measured iron signals. The plan was to carry out five different measurements: one for a normal run (grinder was not used), one with the grinder in the same room as the XRF, one with the grinder in the room next to the XRF room, one with the grinder in the same room as the XRF but plugged in the other room (using an extension cord), and lastly with the grinder in the other room but plugged in the same room as the XRF (using an extension cord).

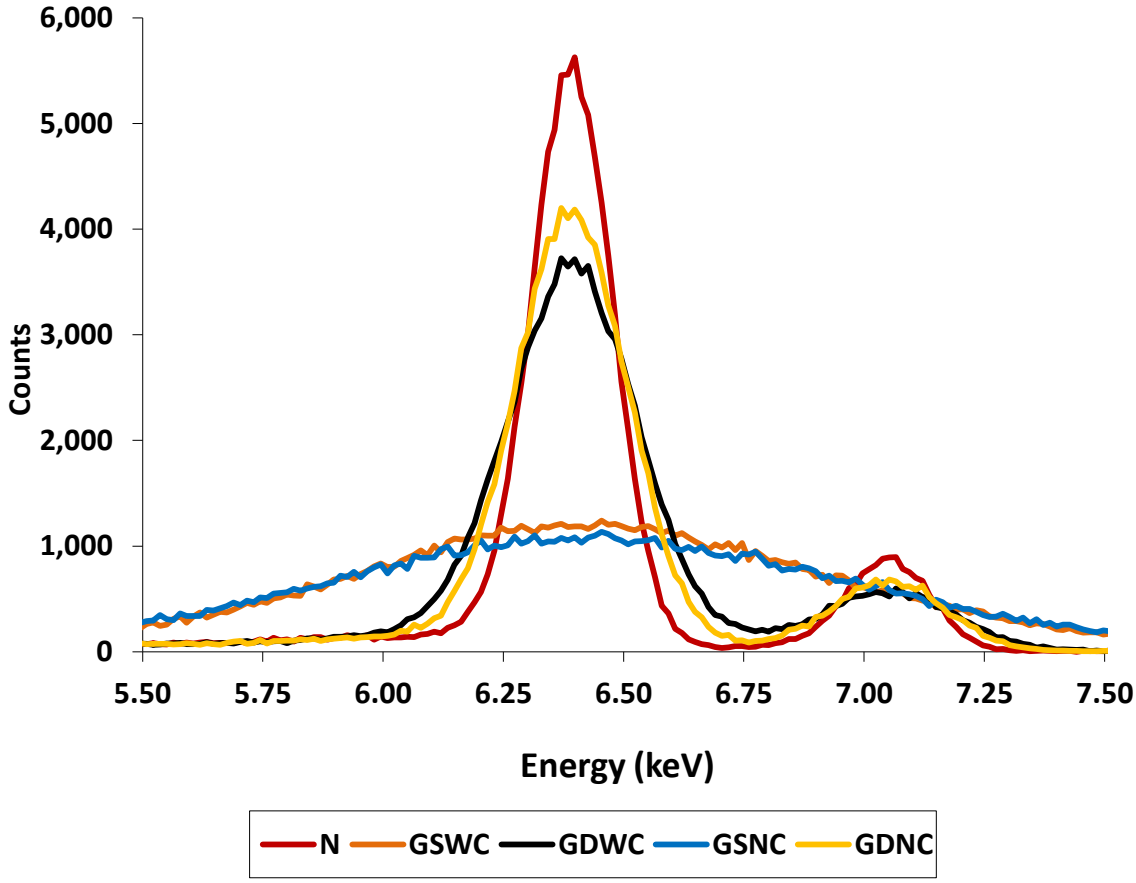

Figure 3.9: Maestro spectra of **N:** Normal run, **GSWC:** Grinder in Same room With extension Cord, **GDWC:** Grinder in Different room With extension Cord, **GSNC:** Grinder in Same room with No extension Cord, **GDNC:** Grinder in Different room with No extension Cord. A steel block was used as a target. X-ray tube settings were 37.5 kV for voltage and 0.6 mA for current. Each measurement was done for a live time of 60 seconds. Whenever the grinder was to be used, it was run for the entire 60 seconds of the experimental time.

From Oxford English dictionary, the word "interference" in physics is defined as "the combination of two or more electromagnetic waveforms to form a resultant wave in which the displacement is either reinforced or cancelled", or "the fading or disturbance of received radio signals caused by unwanted signals from other sources, such as

unshielded electrical equipment". [38] The unwanted signals in this case were the electromagnetic waves that were produced by the grinder. These waves would have various effects on collected data, ranging "from a simple degradation of data to a total loss of data". [39] This is very evident as seen in figure 3.9. The grinder had the greatest effect on the signal when it was used in the same room as the XRF – whether it was plugged in the same room or in a different one. The influence was reduced when the grinder itself was used in a different room; however, the influence was still present.

There are two options to overcome this problem. The first one is to build a shielding system around the XRF system (which would be expensive and time consuming), and the second option is to work after regular working hours (after 4pm). This option would ensure that most researchers have left the building, thus, minimizing the usage of instruments. Option two was chosen, and all measurements in this study, from this point, were done after 4 pm.

3.8. Testing the Effect of Rise Time: Second Attempt

The methodology used to re-measure the effect of rise time was carried out as it was outlined in section 3.6.

As seen in figure 3.10: (a) there is a clear trend between FWHM and rise time. As the rise time increases, the FWHM decreases until it starts leveling off at about 10 μs. Figure 3.9: (b) shows a positive linear relationship between dead time and rise time. Since there is not much of a difference between the FWHM at 9 μs and that at 10 μs, 9

µs was chosen as the rise time to reduce the dead time even more. Dead time was kept at ~ 10 – 12%

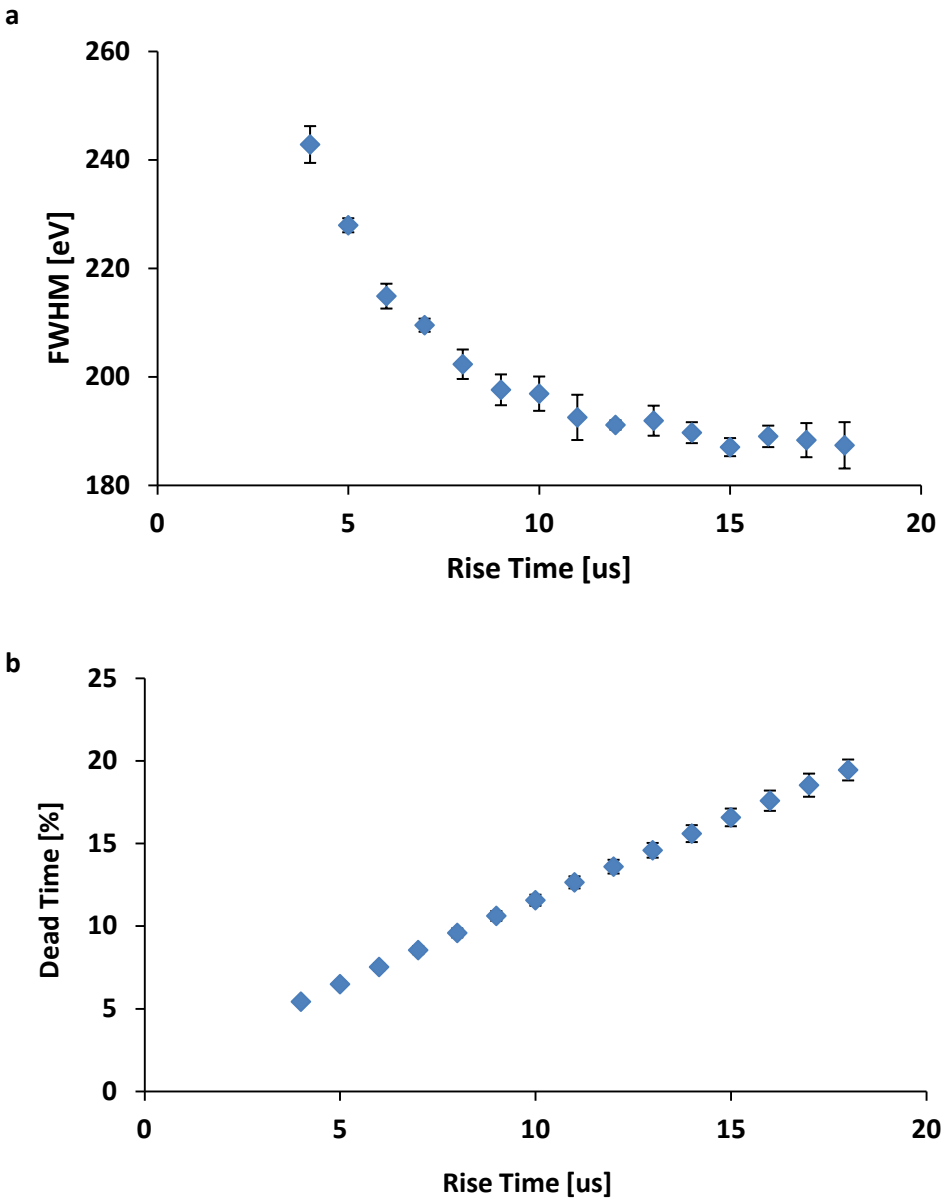

Figure 3.10: a: FWHM as a function of rise time. b: dead time as a function of rise time. Each measurement was done for 30 seconds live time. The voltage was 30 kV and the current was 0.5 mA.

3.9. Iron Concentration Calibration Graph: Second Attempt

For the second attempt, it was decided to test water phantoms for a longer time period (3600 s live time) and higher iron concentrations. The following concentrations were prepared: 0, 25, 50, 100, 400, 683, and 1000 ppm. Each water phantom was measured twice.

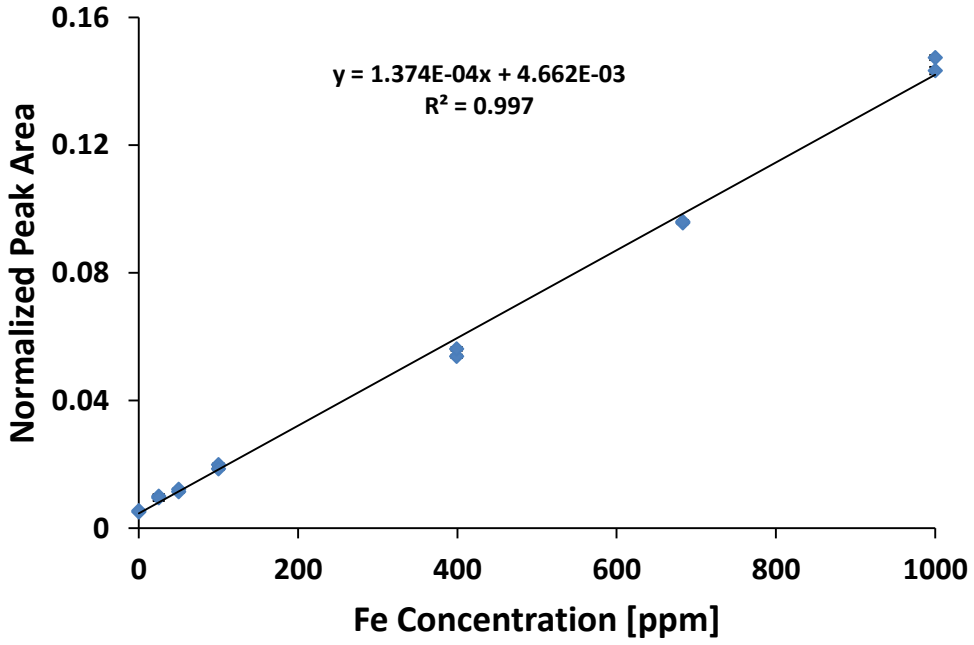

Figure 3.11: Calibration graph of normalized iron peak areas as a function of iron concentration. Error bars are very small to be seen. The voltage was 37.5 kV and the current was 0.6 mA.

Figure 3.11 shows a huge improvement of the calibration line compared to figure 3.6. There is a clear linear relationship between the signal intensity and the iron concentration. The R^2 value is 0.997, which is considered to be very good.

3.10. Geometry Change

It was decided to bring the detector closer to the x-ray tube, so the beam travels a shorter distance before hitting the target, thus a stronger flux by a factor of $1/r^2$ could be achieved. A 12.9 cm copper tube was used instead of the 31.3 cm aluminum tube. Another feature added to the system was a protection cap to ensure the detector's fragile beryllium window did not get damaged. The top part of the cap was made of a square aluminum sheet with a 1.0 cm diameter hole at its centre (the same size as the crystal), as seen in figure 3.12.

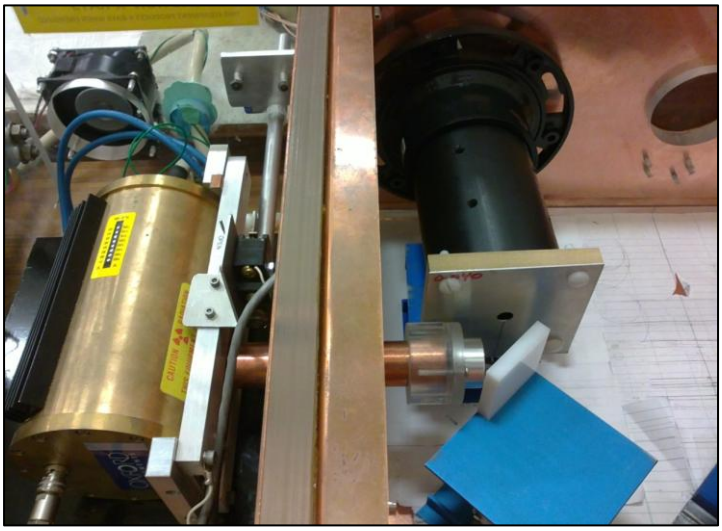

Figure 3.12: Picture of the XRF system after few changes. The length of the x-ray tube plus the collimator is 15.3 cm (compared to 33.7 cm previously). A protection cap was added to the detector.

3.11. Iron Concentration Calibration Line after Geometry Change

Since this was considered to be the last calibration line to be done, the focus was on measuring lower concentrations: 0, 10, 20, 30, 40, 50, 75, 100, 125, and 150 ppm. Samples were measured for longer times compared to those previously. 0, 10, and 20 ppm were measured for 10800 second live time; 30, 40, 50, and 75 ppm for 7200 second; and 100, 125, and 150 ppm for 3600 second (since they have much larger signal intensities).

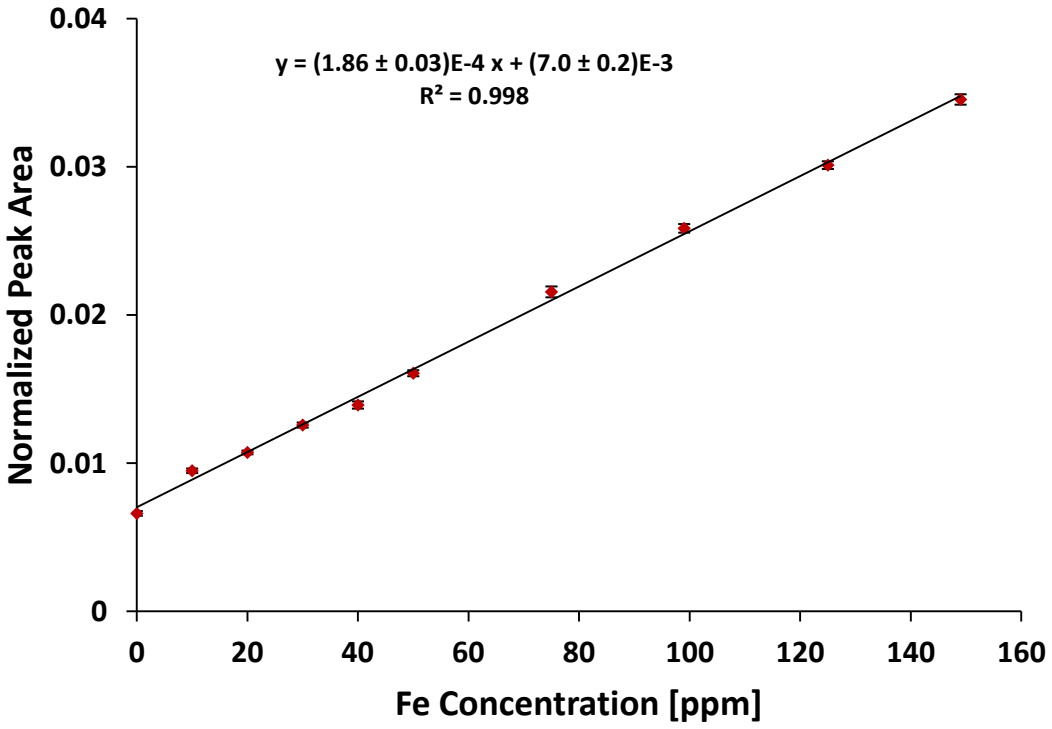

Figure 3.13: Calibration graph of normalized iron peak areas as a function of iron concentration after system geometry change. The voltage was 30 kV and current was 0.5 mA.

From figure 3.13, the equation of the best fit line from the calibration graph is:

$$y = (1.863 \times 10^{-4} \pm 0.028 \times 10^{-4}) * x + (7.01 \times 10^{-3} \pm 0.22 \times 10^{-3}) \quad (3.1)$$

When measuring the mice tissues, the "y" value will be obtained from these measurements and the "x" value (concentration) will need to be calculated. Eq 3.1 is rearranged:

$$x = \frac{y - 7.01 \times 10^{-3}}{1.863 \times 10^{-4}} \quad (3.2)$$

Another important concept to be discussed before carrying out the mice tissue experiment is the minimum detectible limit (MDL). MDL is calculated based on the calibration line found in figure 3.13: [40, 41]

$$MDL = 2\sigma_{xexp} \quad (3.3)$$

where

$$\sigma_{x_{exp}}{}^2 = \left(\frac{\sigma_{y_{exp}}}{m}\right)^2 + \left(\frac{\sigma_b}{m}\right)^2 + \frac{\sigma_m{}^2 (b - y_{exp})^2}{m^4} + 2\left(\frac{y_{exp} - b}{m^3}\right)\left(-\frac{\sigma_y{}^2 \sum_{i=1}^{N} x_i}{D}\right) \quad (3.4)$$

m is the slope and σ_m is its error, b is the y-intercept and σ_b is its error, y_{exp} is the value of the normalized area of the 0ppm phantom and σ_{yexp} is its error. σ_y is found as shown in eq. 3.5 and D in eq. 3.6:

$$\sigma_y{}^2 = \frac{\sum_{i=1}^{N} [y_i - (mx_i + b)]^2}{N - 2} \quad (3.5)$$

$$D = N \sum_{i=1}^{N} x_i^2 - \left(\sum_{i=1}^{N} x_i\right)^2 \quad (3.6)$$

It was found that the MDL of this XRF system, with this particular geometry, for iron in water phantoms was 2.9 ppm.

To test the reliability of the calibration line from figure 3.13, a standard was measured with a known iron concentration. Non defatted lobster hepatopancreas reference material for trace metals (LUST-1, National Research Council Canada) has an iron concentration of 11.6 ± 0.9 ppm as bottled and 77.8 ± 6.0 ppm dry weight. The measured sample from the standard in the XRF system gave an iron concentration of 14.2 ± 2 ppm, which is in agreement with the standard (bottled) when taking uncertainties into consideration. The slight elevation of iron concentration in the measured sample (compared to the standard) is because the sample was measured for 18000 second and thus there was a slight dehydration of the sample, and as a result, an increase of iron concentration.

Chapter 4: Iron levels in the Skin, Liver and Heart of Mice

The Livers, skins and hearts of control mice were provided for this study. The mice strain was 3XTg-AD and their age ranged from 5 – 13 months. The liver was the left lobe of the organ, while the skin was shaved (to reduce the amount of hair) and cut from the belly area, whereas the heart was the whole organ.

4.1. Sample Preparation

Same phantom holders that were used for water phantoms were also used for this part of the experiment. Firstly, silicon paste was spread around the hole, and then the sample was carefully place inside that hole. A piece of XRF film was tightly pressed against the holder's surface to ensure that the sample was secured in place with no fluid leakage (figure 4.1). Sample preparations were carried out inside a biosafety cabinet.

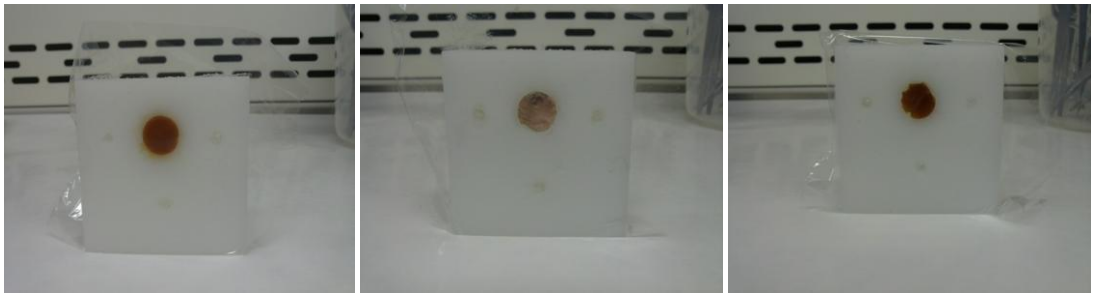

Figure 4.1: Heart, skin and liver samples in sample holders

4.2. Sample Measurements

In this experiment, each organ was measured in the same setting as the last calibration line. The voltage was set to be 30 kV, whereas the current was 0.5 mA. Each sample was measured for a different live time to ensure that at least 10,000 counts were obtained under each iron peak. Overall most liver samples were measured for 2 hours (7200 sec), 3 hours (10800 sec) for the heart, and 6 hours (21600 sec) for the skin. After obtaining the spectra, areas under the iron peaks were normalized to live time. Iron concentrations were calculated (eq. 3.2) and summarized in Table 4.1.

Mouse #	Liver	Heart	Skin	Mouse #	Liver	Heart	Skin
1	113 ± 2	71 ± 2	26 ± 1	**19**	192 ± 3	51 ± 2	5 ± 1
2	45 ± 2	40 ± 2	16 ± 1	**20**	144 ± 3	44 ± 2	8 ± 1
3	150 ± 3	39 ± 2	6 ± 2	**21**	137 ± 3	48 ± 2	12 ± 1
4	143 ± 3	55 ± 2	4 ± 1	**22**	152 ± 3	37 ± 2	9 ± 1
5	100 ± 2	81 ± 2	38 ± 2	**23**	92 ± 2	49 ± 2	1 ± 1
6	72 ± 2	34 ± 2	3 ± 1	**24**	100 ± 2	31 ± 2	5 ± 1
7	115 ± 2	57 ± 2	13 ± 1	**25**	164 ± 3	83 ± 2	9 ± 2
8	305 ± 5	89 ± 2	8 ± 1	**26**	188 ± 4	73 ± 2	25 ± 1
9	37 ± 2	40 ± 2	3 ± 1	**27**	257 ± 4	61 ± 2	11 ± 1
10	75 ± 2	35 ± 2	1 ± 1	**28**	86 ± 2	62 ± 2	11 ± 1
11	76 ± 2	44 ± 2	5 ± 1	**29**	97 ± 2	46 ± 2	14 ± 1
12	64 ± 2	35 ± 2	1 ± 1	**30**	101 ± 3	37 ± 2	7 ± 1
13	94 ± 3	40 ± 2	3 ± 1	**31**	125 ± 3	37 ± 2	2 ± 2
14	61 ± 2	35 ± 2	10 ± 1	**32**	158 ± 3	75 ± 2	36 ± 2
15	52 ± 2	36 ± 2	6 ± 1	**33**	136 ± 3	33 ± 2	0 ± 2
16	208 ± 4	79 ± 2	16 ± 2	**34**	129 ± 3	42 ± 2	2 ± 1
17	96 ± 2	48 ± 2	4 ± 1	**35**	118 ± 2	58 ± 2	22 ± 1
18	234 ± 4	59 ± 2	9 ± 1	**36**	87 ± 2	40 ± 2	8 ± 1

Table 4.1: Calculated iron concentrations [ppm] in measured mice tissues

From table 4.1, 6 skin samples had iron concentrations lower than the MDL of 2.9 ppm. The average of iron concentration in skin was 9.8 ± 1.6 ppm and the range was -2 – 38 ppm. These results are in agreement with literature reports as stated in the introduction (these studies were conducted on humans rather than mice, however). The negative values are the result of the uncertainty in the background measurement. The liver had the greatest range, 37 – 305 ppm, and an average of 125 ± 10 ppm. The range value is wider than what was found in the Parr *et al.* [30] study (42 -252 ppm); however, taking uncertainties into consideration, the average concentration is in agreement with their value of 183 ± 86 ppm and also in agreement with the average from Wittaker *et al.* [34] (112 ± 5 ppm). The heart had a range from 31 – 89 ppm and an average of 50.7 ± 2.7 ppm, which are in agreement with the average of 48.2 ± 0.5 ppm from Milstone *et al.* [31] study. The reason behind these wide ranges is because the mice ages had a wide range as well (5 – 11 months). Adams *et al.* [42] stated that iron levels increase over time (age) in control animals.

a

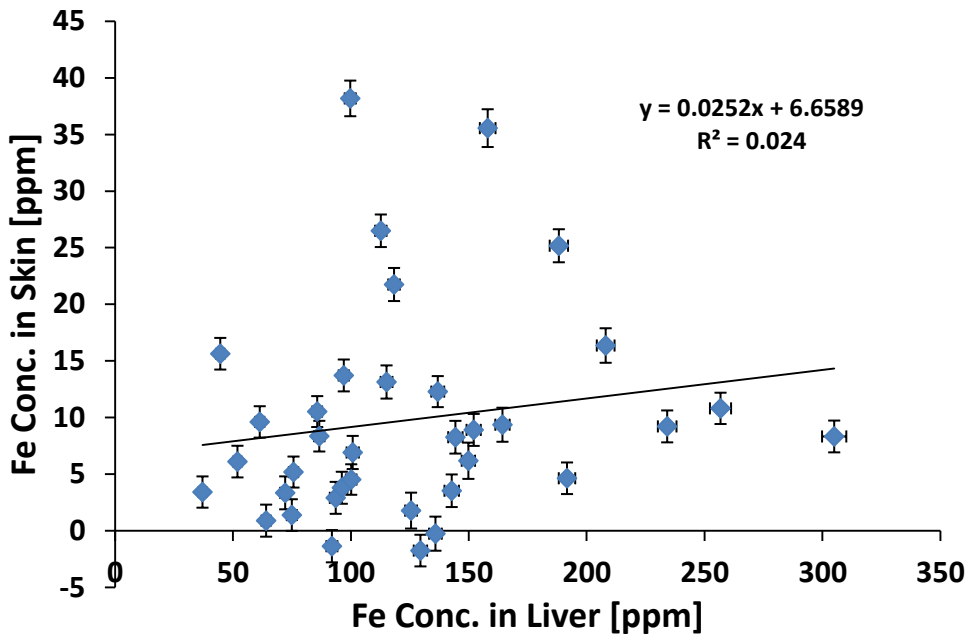

b

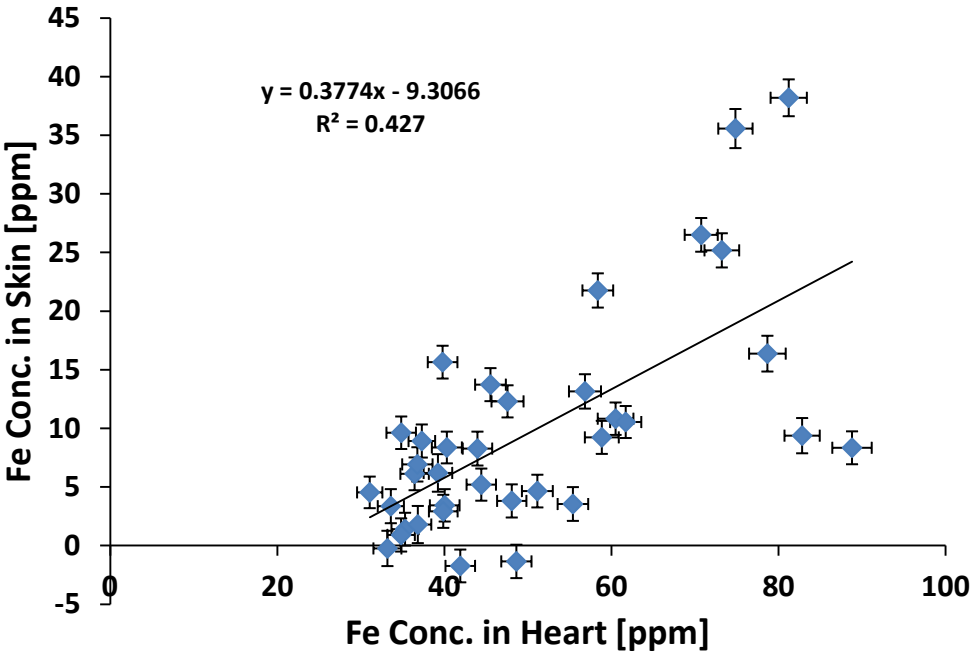

Figure 4.2: a: iron concentration in the skin vs in the liver. **b:** iron concentration in the skin vs in the heart

Figure 4.2: (a) shows a very weak correlation between iron levels in the skin compared to levels in the liver. The R^2 value was only 0.025. Testing the significance of this correlation, the p-value was found to be 0.36, which indicates that it is not significant. On the other hand, figure 4.2: (b) shows a much stronger correlation. The R^2 value was 0.427 and the p-value < 0.01. This indicates that the correlation between the iron levels in the skin and the heart is significant.

When testing the normality of the skin, heart and liver, the p-values (Shapiro-Wilk test) were <0.01, <0.01, and 0.02 respectively. This shows that only liver data were significantly normal. The lack of normality indicates that Pearson's correlation coefficient (figure 4.2) is not appropriate to be used in this case. Spearman's rank correlation coefficient was calculated instead. For skin vs liver, the R_s^2 value was 0.080 and the p-value = 0.095. For skin vs heart, the R_s^2 value was 0.382 and the p-value <0.01. The results from Spearman's rank correlation coefficient are comparable to what was measured with the Pearson's correlation. In both methods, it was found that the correlation is significant between the iron levels in the skin and the heart but not between the skin and the liver.

The overall results discussed above do not agree with the strong correlation reported by Farquharson *et al.*[25] As stated in the introduction, Farquharson and his team found the R^2 values, from iron levels in skin vs. liver and skin vs. heart, to be 0.86 for both. However, looking closely at the plots provided by Farquharson *et al.* [25] (figure 4.3) the correlation between the iron in the skin and the other two organs at low

concentrations is not visible (however, it is clear at higher concentrations). Farquharson *et al.* used rats that were iron-loaded to closely resemble β-thalassemia patients. As stated earlier, the mice used in this study were control mice, with no iron overload. Also, it can be seen that all the values obtained from table 4.1 (whether it is iron levels in the skin (<40 ppm), the liver (<1000 ppm) or the heart (<100 ppm)) lie within the low concentration ranges of the Farquharson *et al.* study.

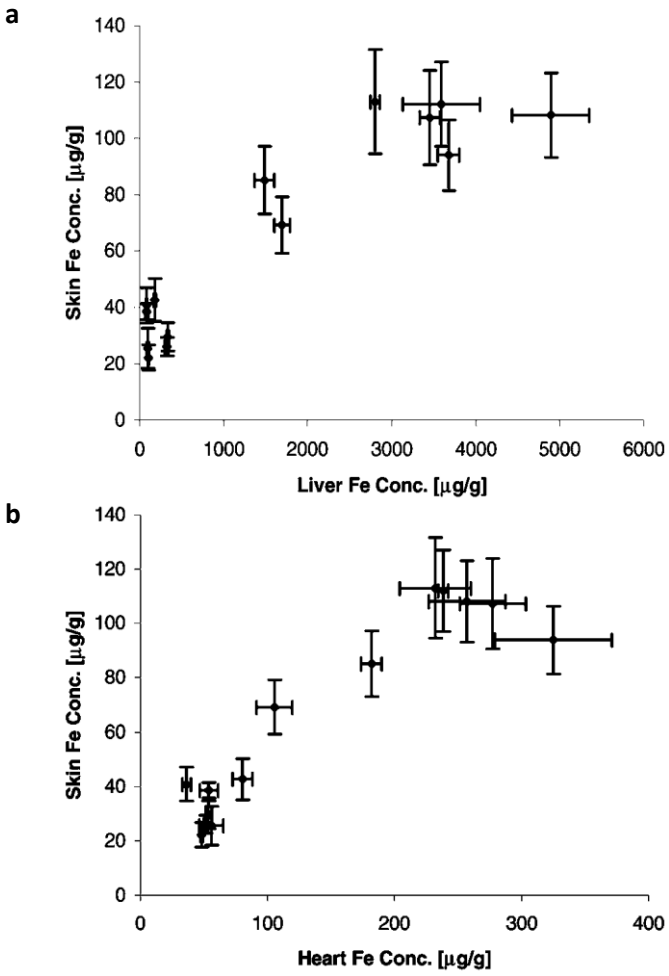

Figure 4.3: Correlation between iron concentrations in the skin and in the **a:** liver and **b:** heart from Farquharson *et al.* [25] study.

Chapter 5: Iron in Human Skin

Skin is a heterogeneous organ. It is "composed of liquids, connective tissues, muscle fibers and various glands". [23] Thus, it is most likely that iron will have a non-homogeneous distribution across the different layers of skin.

It is worthwhile to investigate the distribution of iron levels in human skin. One of the techniques that could be used is by using synchrotron radiation.

5.1. Collecting Human Skin Specimens

The Hamilton Health Science Human Tissue Committee, a sub-committee of the HHS/FHS Research Ethic Board approved collection of skin specimens from deceased persons donated for scientific research. Samples were obtained from the Anatomy Department in Hamilton Health Science at McMaster University Medical Centre.

8 mm biopsy punches (Miltex Inc., York, PA) were used to extract 10 different specimens from each cadaver from the following sites: chest, back, right palm, left palm, right upper arm (medial), left upper arm (medial), right thigh (medial), left thigh (medial), right foot and left foot. Specimens were kept frozen at -75°C until needed.

The chest, back, and all samples from the left side of the body were preserved for the synchrotron study.

5.2. XRF Measurements

The samples from the right side of the body were used to measure iron concentrations in the XRF system with the same procedure used for the mice samples (discussed in chapter 4). Sample preparation procedure was carried out the same as is outlined in section 4.1. All samples were measure for 21,600 seconds live time and at least 10,000 counts was obtained for each measurement. 30 kV was used for tube voltage and 0.5 mA for the current. Table 5.1 summarizes these measurements.

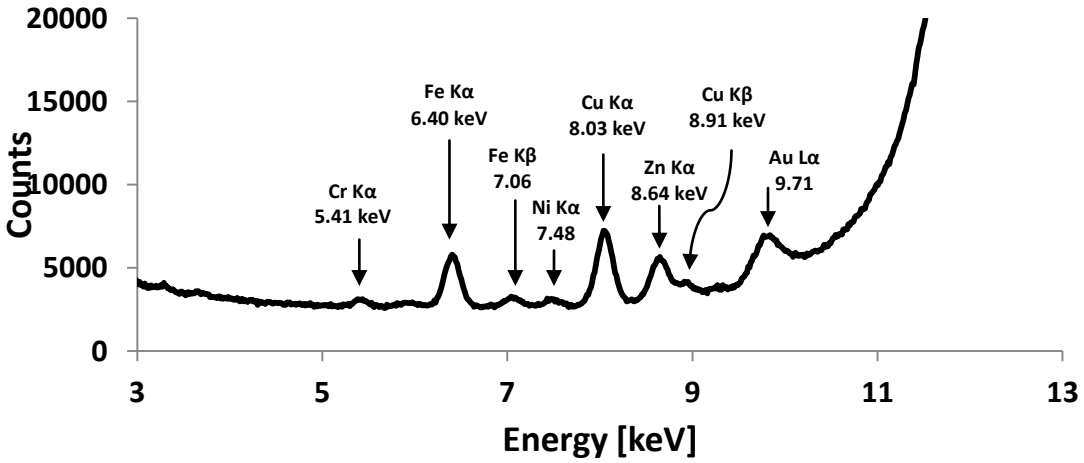

Figure 5.1: Maestro spectrum of a human skin sample. X-ray tube settings were 30.0 kV for the voltage and 0.5 mA for the current. This particular sample was measured for 122,000 sec live time (33.89 hrs)

Figure 5.1 represents a typical human skin spectrum. As expected, Fe Kα is present as well as Cu Kα and Au Lα. Fe Kβ and Cu Kβ are present because this sample was measured for a very long time, otherwise, they would not be detectable (very low intensity) if it was measured for a shorter time. Despite the fact that the main contributor of Cu signals is the copper shielding of the system, it was reported that Cu

is present in the skin. Another element that is found in human skin with a sizeable peak is Zn Kα at 8.64 keV. For a 33.89 hrs measurement, Cr Kα (at 5.41 keV) and Ni Kα (at 7.48 keV) peaks are considered too small for any further consideration.

Body Part	Body 1	Body 2	Body 3	Body 4	Body 5	Body 6
Arm	59 ± 2	1 ± 1	0 ± 2	1 ± 1	3 ± 1	20 ± 2
Foot	9 ± 1	0 ± 1	-3 ± 1	4 ± 1	5 ± 2	3 ± 1
Palm	3 ± 1	0 ± 1	2 ± 1	1 ± 1	-2 ± 1	1 ± 1
Thigh	3 ± 1	3 ± 2	0 ± 1	4 ± 1	-1 ± 1	5 ± 1

Table 5.1: Iron concentrations [ppm] in skin from different body parts from 6 different cadavers

From table 5.1, there was one sample (1-arm) which had an iron concentration that was a lot higher than the other measured samples. This is possibly due to contamination (most likely from air dust). Samples 3-foot, 5-palm and 5-thigh showed negative results. The negative values are the result of the uncertainty in the background measurement. The average iron concentration in all measured human skin samples was 5 ± 3 ppm (with a median of 3 ppm). 12 out of the 24 samples measured showed a concentration that is less than the MDL of 2.9 ppm. It seems that most skin samples measured in this study had iron concentrations at the lower values of the reported ranges. As stated in the introduction, few studies showed that the average iron concentration in the skin of normal individuals was 11 ppm. However, most of the previous studies were performed on living individuals, whereas this one used specimens collected from deceased bodies. Gorodetsky *et al.*[23] stated that when

biopsies are extracted "they may manifest microchanges in a tiny area of the skin rather than the average concentration at the examined location".

5.3. The Problem with Normalizing Iron Peaks to Scatter Peaks

Initially, scatter peaks were used for normalizing the measured iron peaks in water phantoms, mice and human samples. However, the majority of the calculated iron concentrations in human skins were negative, which indicated that these normalized iron peaks were not calculated correctly. Measured iron and scatter peaks were further investigated (figure 5.2)

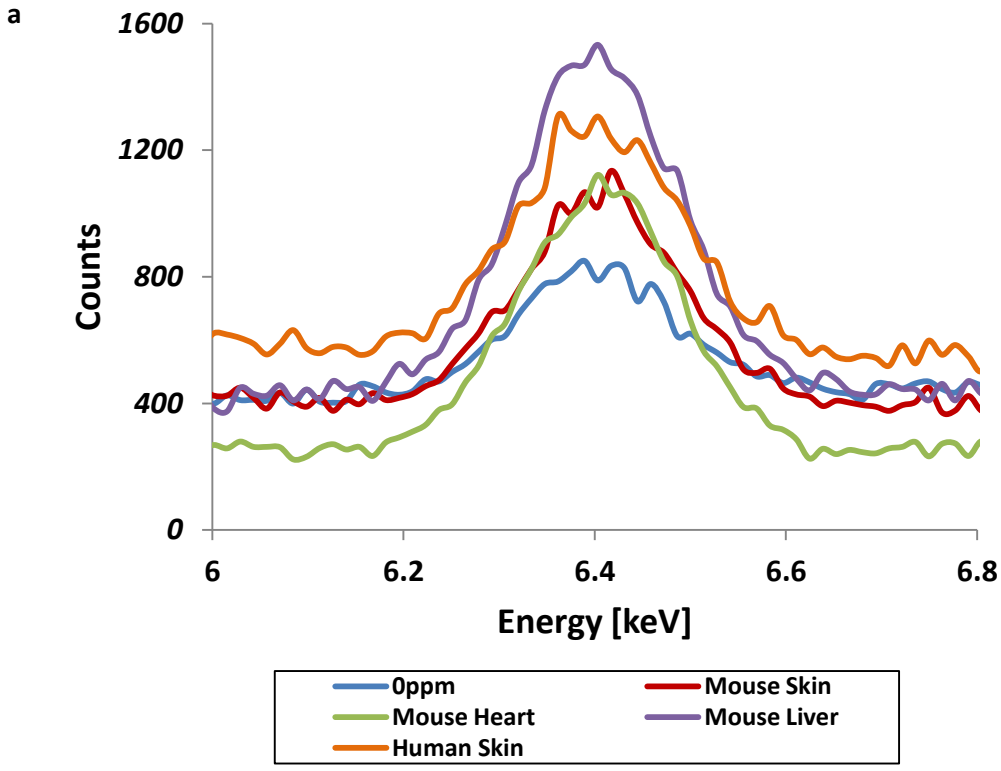

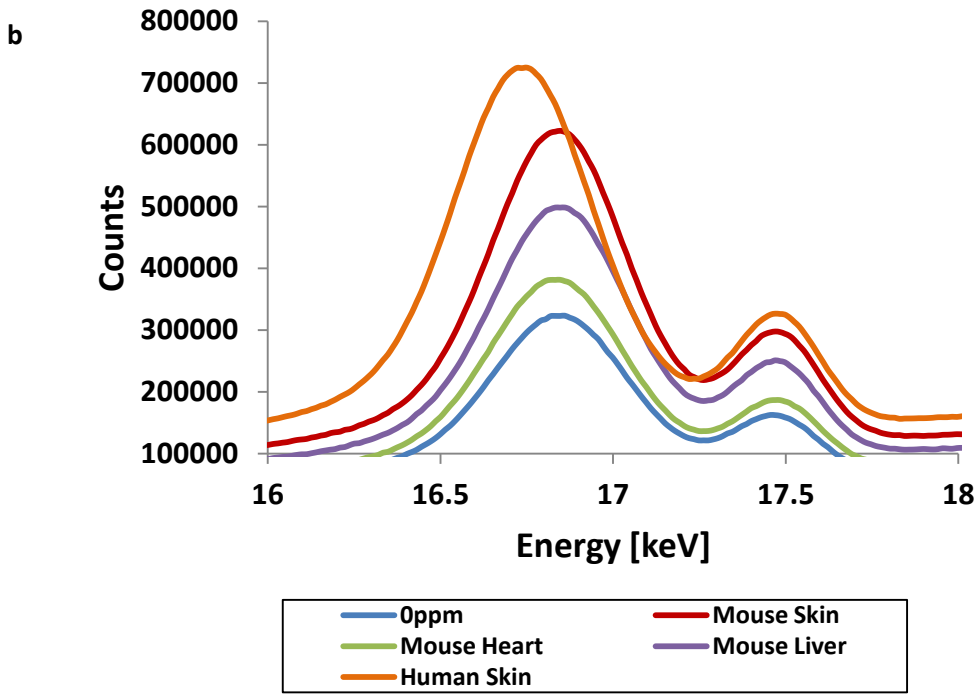

Figure 5.2: spectra of **a:** iron peaks **b:** Compton and coherent scatter peaks of Mo Kα photons

In figure 5.2, a human skin spectrum was plotted against the 0 ppm and the mice skin, liver and heart spectra to compare the positions of their iron and scatter peaks. Form both plots, iron and coherent peaks of all samples were lined at where they should be; 6.4 keV and 17.48 keV respectively. However, for the human skin, the Compton peak was not lined with the Compton peaks of the other samples. This shift suggests a change in Compton scattering angle. According to eq. 1.2, any change of the angle θ will result in a different Compton distribution, thus producing Compton peaks with different areas. This is especially sensitive for a system with a 90° geometry (due to the cosine distributions). As a result, scatter peaks were not used for normalization and only scanning time was used for iron peak normalization.

5.4. Sample Preparation for Synchrotron Study

The samples that were preserved for synchrotron study were removed from the freezer and placed (each in its own beaker) in 10% buffered neutral formalin (VWR LLC., Edmonton, AB) for at least 24 hours at room temperature. After that, each sample was cut into two halves and placed back in the formalin solution for another 24 hrs (the purpose of formalin is to fix the samples to prevent them from decaying or degeneration and to eliminate any biological hazards when used at room temperature). On the next day, these samples were transferred to 70% ethanol solution and were sent to the histology lab in Michael G. DeGroote Centre for Learning and Discovery at McMaster University. The fixed samples were embedded in paraffin wax and sliced into 10 μm sections, which were then mounted on thin XRF film holders to be examined. This process was done in a way that ensured that all skin layers were sitting flat on the film.

5.5. Trace-Elements Distribution in Skin Layers: Previous Studies

The importance of various elements in the skin has encouraged scientists to develop techniques and instruments to be used in measuring the distribution of these elements across the different layers of skin. Measurement of iron in the skin has been investigated as early as the 1970s of the last century. [43] The most extensive work on trace element distribution across human skin layers was done by Bo Forslind *et al.*[44-48] Table 5.2 is taken from Forslind *et al.*[47] study (a scanning nuclear microprobe

method was used) and it shows the Ca, Fe, and Zn distribution across the various layers of epidermis of normal skin.

Element	Basale	Spinosum	Corneum
Ca	320.3 ± 150	231.7 ± 158.4	350.1 ± 199.4
Fe	105.5 ± 84.93	36 ± 46.82	16.6 ± 26.27
Zn	23.12 ± 46.76	46.67 ± 65.82	27.74 ± 46.77

Table 5.2: Trace elemental distribution over skin cross section [ng/mg]

Table 5.2 shows that the Ca level peaks in the corneum and basale strata. The Fe level peaks in the epidermis's deepest layer (Basale) and decreases towards the skin surface. For Zn, the highest concentration is in the middle layer, the spinosum. However, taking uncertainties into consideration, Ca and Zn levels seem to be consistent in all three layers, whereas it is not the case with iron.

In this synchrotron study, Ca and Zn will be closely examined, along with Fe, so it would be easier to identify the skin layers, as well as to confirm previous studies. Also, it should be noted that no medical information was provided regarding the cadavers used. Thus, they are assumed to be control samples.

5.6. Synchrotron- Canadian Light Source (CLS)

A synchrotron light source is a large particle accelerator that produces brilliant light that is used in physical, chemical, biological, and geological research. The basic outline of synchrotron function is as follow: an electron gun is used to supply electrons to a Linear Accelerator (LINAC), where radio frequency waves are used to accelerate these electrons to nearly the speed of light. The electrons are then injected into a huge

donut-shaped tube called the ‘storage ring’. A series of magnets are used to bend the trajectory of the electrons in a circular orbit. This process will naturally cause the electrons to emit a highly focused, brilliant light. This phenomenon is called ‘synchrotron light’. Different spectra of this synchrotron light (IR, UV, and x-rays) will be piped to tangential straight tubes, which are called ‘beamlines’, where experimental work occurs. [49-51]

There is only one synchrotron facility in Canada (Canadian Light Source), which is located at the University of Saskatchewan in Saskatoon, SK.

The beamline that was used for this study is called ‘VESPERS’ (Very powerful Elemental and Structural Probe Employing Radiation from a Synchrotron).[52] This beamline was designed in a way to “deliver a micro-focused hard X-ray beam to solid materials in such a manner that a microscopic volume can be analysed by X-ray Diffraction (XRD) analysis and X-ray Fluorescence (XRF) spectrometry… it should also be possible to obtain X-ray Absorption Spectrometry (XAS)”.[53] Only XRF was used in this study.

A silicon drift detector (SDD) is used in this system, which has a 400 µm silicon wafer, an active area of 50 mm^2 and a 12.5 µm Be window (SII NanoTechnology, California). An aluminum sample holder was placed at a 45° angle to the detector and 180° to the beam source (beam size is 6x6 µm in diameters). The holder will position the samples at a 45° from the vertical plane and at a distance of 3 cm away from the detector (figure 5.3).

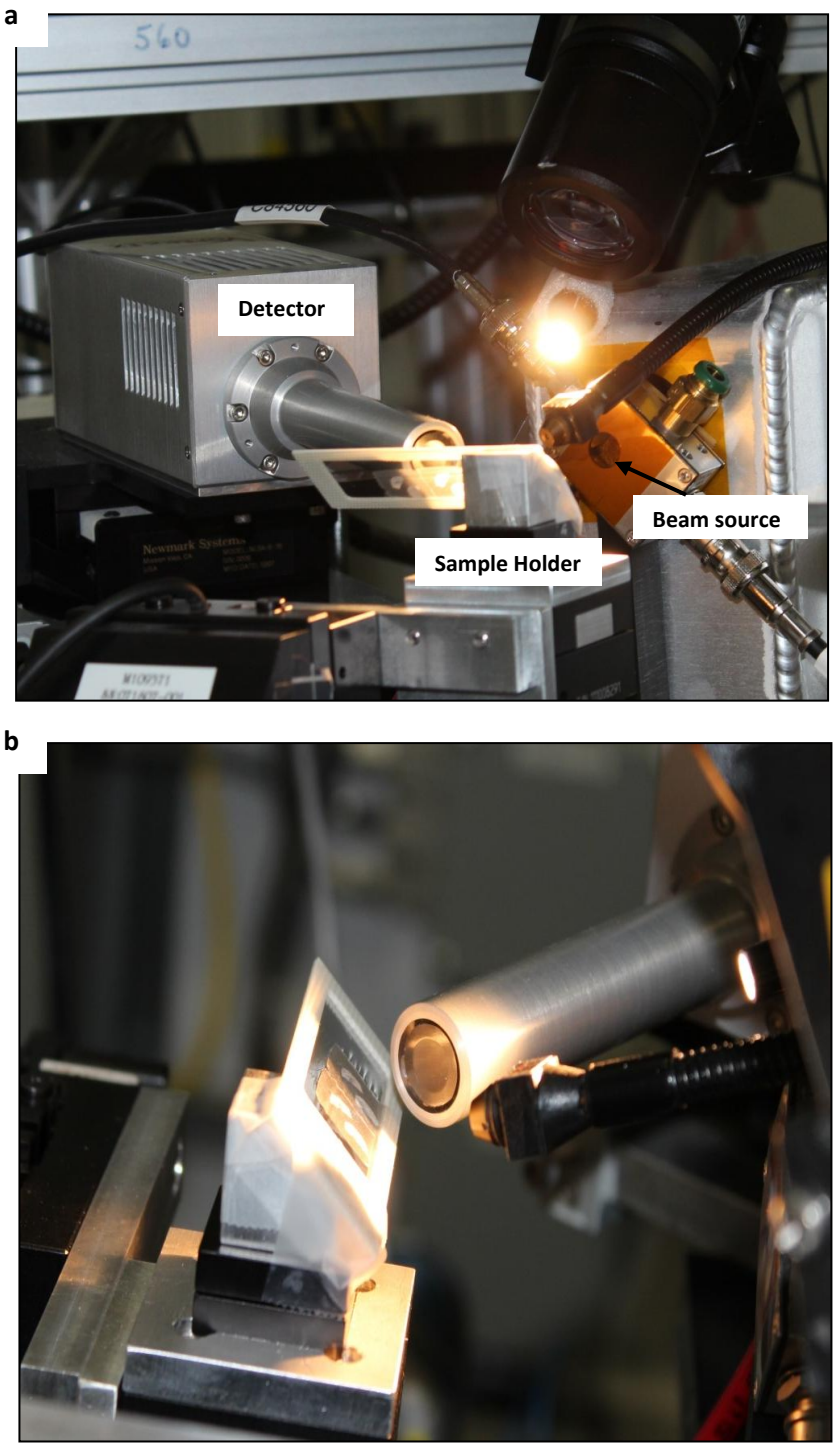

Figure 5.3: a: VESPERS beamline setup at CLS. **b:** Samples are positioned at a 45° to the vertical plane and 45° to the detector at a distance of 3 cm.

5.7. Trace-Elements Distribution in Skin Layers: CLS Experiment

In this experiment, the x-ray beam was targeted towards cross sections of various prepared humans skin samples to obtain detailed maps of elemental levels as a function of depth. The beam moved at incremental steps of 10 μm in both the x and y directions (each measured pixel is 10x10 μm in dimension). For each pixel, a spectrum was collected showing the elements present in each sample. The number of pixels measured varied from sample to sample, depending on the region of interest determined by the researchers. In this research, a total of 18 scans were collected. Beam energies of 8 keV (4 samples), 12 keV (11 samples) and 13 keV (3 samples) were used.

MATLAB's Curve-Fitting Toolbox (cftool) was used to measure the peak areas of Fe, Ca and Zn and were normalized using the total areas of the scattering peaks (both Compton and coherent) in order to correct for beamline intensity drops over the duration of a single scan. The normalized peak areas were then used in Interactive Data Language 6.2 or "IDL 6.2" (Exelis VIS, Boulder, Colorado) for distribution mapping (figure 5.4).

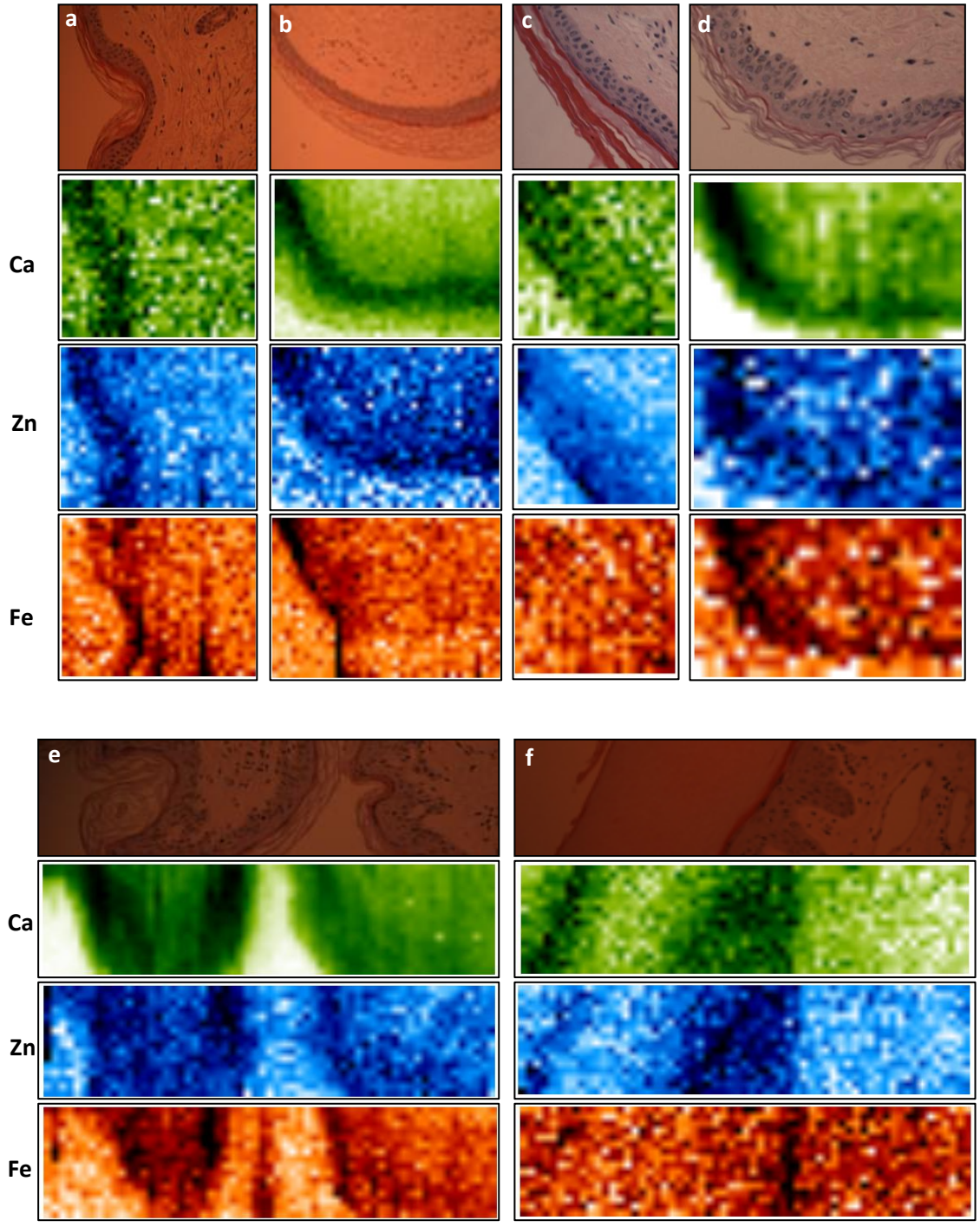

Figure 5.4: Examples of H&E images of skin samples and the corresponding Fe, Zn and Ca maps in IDL. The darker the colour, the higher the concentration. For all shown images, scan time was 20 sec/ pixel. Beam energy was 12 keV for all but the palm (13 keV). **a:** 300x250 µm scan of a thigh sample, **b:** 350x250 µm scan of an arm sample, **c:** 200x200 µm scan of another thigh sample from a different cadaver, **d:** 250x150 µm scan of a back sample, **e:** 600x150 µm scan of another back sample from a different cadaver and **f:** 600x150 µm scan of a palm sample.

As seen in figure 5.4, it is very difficult to identify the location of each element in terms of epidermal sub-layers. This could be because the beam step size might have been larger than some of the sub-layers scanned. Also, it is most likely that some scanned pixels were in an overlapping region between these sub-layers, thus giving the average concentrations of the elements in that area. Nonetheless, patterns of elemental micro-distribution can be seen in maps from figure 5.4 and the distinction between the two bulk skin layers is easily identified.

To gain a better understanding of Ca, Fe and Zn behaviour in skin, one-dimensional profiles, over the length of the entire raster scans, were obtained (Figures 5.5 – 5.7). From these figures, it appears that both Ca and Zn occupy similar ranges of distribution, covering most of the epidermal layer. On the other hand, it is very evident that iron is found at a deeper position within the epidermis with a narrower range compared to the other two elements. Another observation is that the intensity levels of all three elements seemed to drop off at the same location, the epidermal-dermal junction. As stated earlier, it is hard to distinguish between epidermal sub-layers, however, certain comparisons between these results and previous literatures could be drawn. Referring back to table 5.2, there is an agreement that Ca and Zn levels are consistent across all epidermal sub-layers and that iron's highest level is found in the deeper sub-layer (possibly the stratum basale).

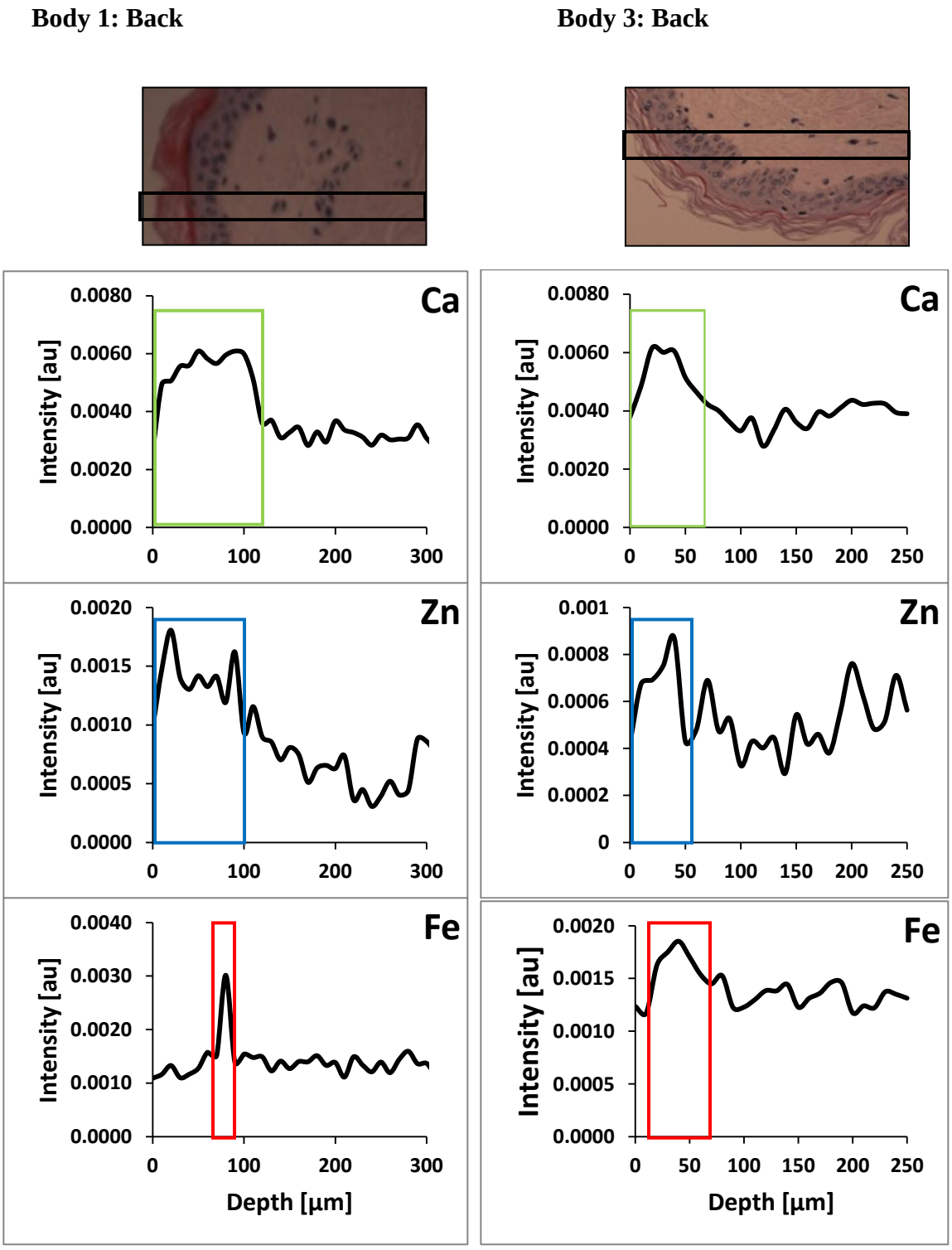

Figure 5.5: 1-D profiles over the length of the raster scan of back samples

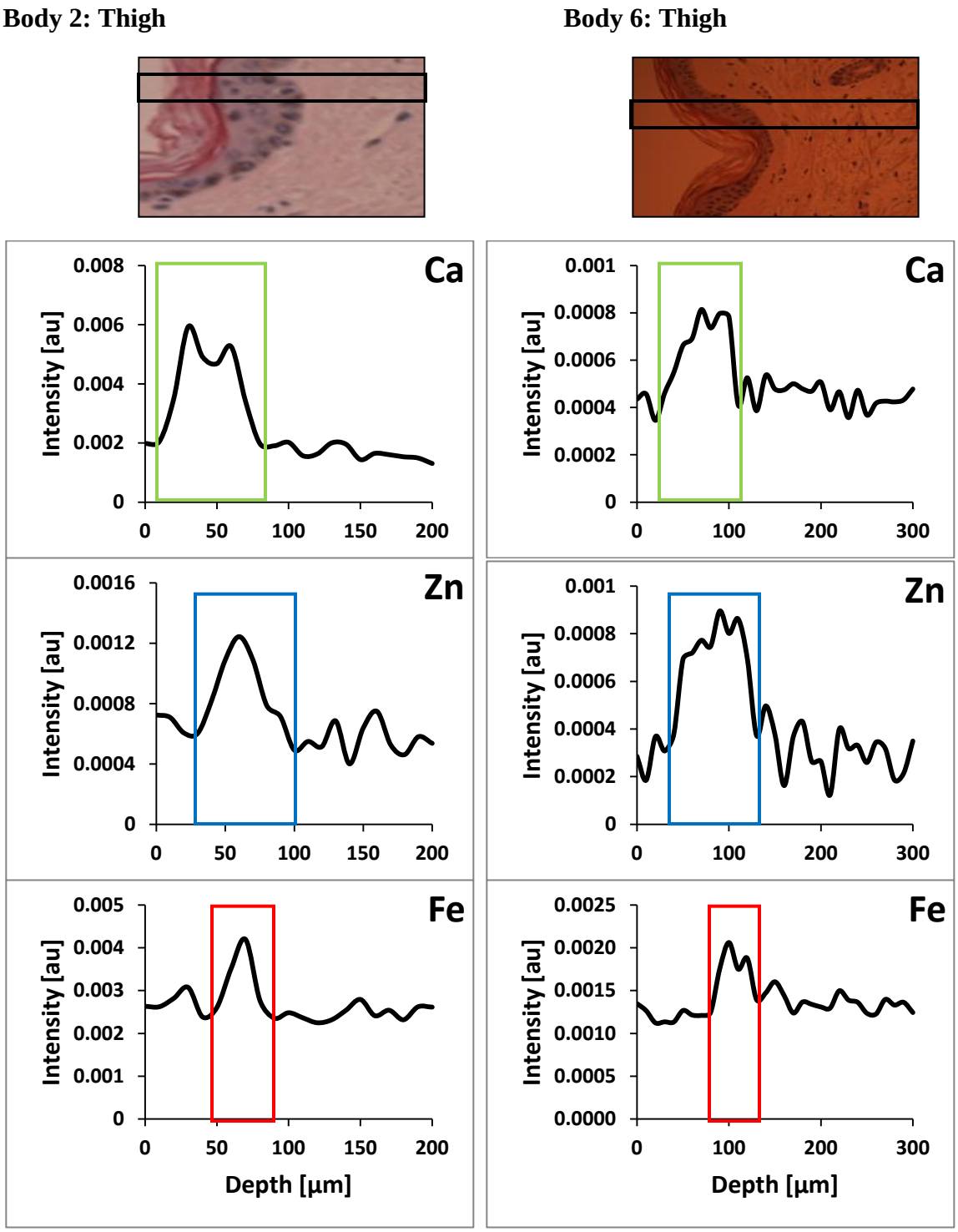

Figure 5.6: 1-D profiles over the length of the raster scan of thigh samples

Body 3: Arm **Body 2: Palm**

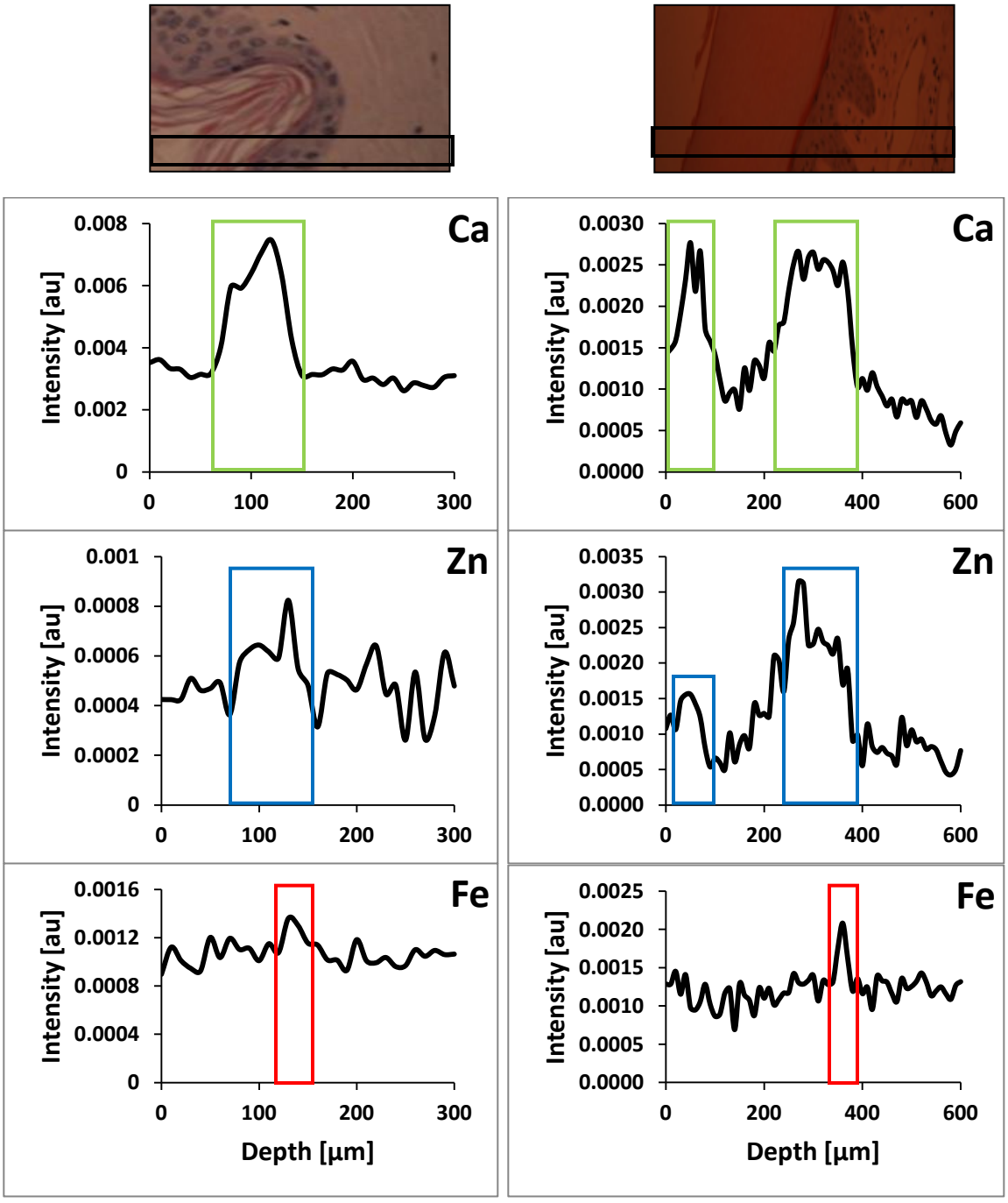

Figure 5.7: 1-D profiles over the length of the raster scans of an arm and a palm samples

Palms have a much thicker stratum corneum, thus it might be easier to identify the elemental presence in various epidermal sub-layers. However, one problem that arose with scanning thick skin in this study was the very lengthy time they required to obtain sufficiently deep scans, thus not many of them were done. One example of a palm scan is represented in figure 5.4 f (and1-D profile in Figure 5.7). Ca and Zn were present in two different regions – closer to the surface and in a deeper layer, but were less in between. The first region (closer to the surface) is clearly the outermost part of the stratum corneum, whereas the next region (with much less elemental levels) represents the rest of the corneum. The reason behind this variation in the croneum is because as the cells move towards the surface, they get dehydrated and more compact, thus elemental levels get enhanced relative to the interior of that stratum. The third region (with high elemental levels) represents both the stratum spinosum and the stratum basale, and the fourth one represents the dermis. In the case of iron, it is only present in the third layer, but with a deeper (at epidermal-dermal boundary) and narrower range compare to the other two elements. This is in agreement with other scans.

Using the start and end points of the calcium distribution in the 1-D depth profiles, the total epidermal thickness was estimated at 70-100 μm (excluding the palm), with an average of 94±5 μm, compared to ICRP 23 values ranging from 34-92 μm. A more accurate measure would have been possible if a sharper fall-off in the calcium distribution were to be noted.

Elemental contamination is not uncommon and is especially true for iron. As stated in the introduction, iron is a very abundant element and is found almost everywhere. Sources of iron contamination include air dust and the contact between a sample slide with any unsterile surface. Thus, extra precaution should be taken when preparing and handling slides. In this study, a few contaminants were detected in the form of hot spots. An example for this could be seen for iron in the arm sample (figure 5.4: b). In this map, it can be seen that as the iron distribution curves towards the right, following the skin shape, there is a straight line of higher iron levels heading downwards into the background. This line is contamination. In addition to this problem, many of the scanned samples showed no trend for elemental distribution at all, especially for iron and zinc. This could be seen for iron in the thigh sample in figure 5.4(c). A reason behind this is because there is a possibility of "postmortem changes in the distribution of trace elements in the tissue" of autopsy samples, as stated by Gorodetsky *et al.*[23] Due to these two limitations, only 14 samples out of 18 were considered for further analysis. Of the remaining four samples, either the raster scans were interrupted due to lack of a clear distribution in elemental levels across all the maps or the completed set of maps did not show such a distribution for two of the three elements investigated (iron and zinc).

In order to establish whether the technique can clearly identify the presence of all three elements in the two layers of the skin – epidermis (layer 1) and dermis (layer 2) – regions of interest were defined for each map. Various statistical hypothesis tests were

preformed to identify if the elemental levels in the epidermis is statistically significant compared to the levels in dermis (table 5.3).

Body	Site	Element	% Difference	p-value
1	Back	Ca	91.6	<0.01
		Fe	44.7	<0.01
		Zn	250.4	<0.01
	Thigh	Ca	93.7	<0.01
		Fe	2.2	0.50
		Zn	268.6	<0.01
2	Thigh	Ca	249.1	<0.01
		Fe	51.9	<0.01
		Zn	166.0	<0.01
3	Back	Ca	86.7	<0.01
		Fe	44.2	<0.01
		Zn	83.8	<0.01
	Chest	Ca	178.4	<0.01
		Fe	7.4	<0.01
		Zn	76.3	<0.01
	Arm	Ca	109.1	<0.01
		Fe	13.1	<0.01
		Zn	33.0	<0.01
4	Back	Ca	117.0	<0.01
		Fe	97.9	<0.01
		Zn	141.1	<0.01
	Arm	Ca	214.9	<0.01
		Fe	113.3	<0.01
		Zn	60.0	<0.01
	Thigh	Ca	297.2	<0.01
		Fe	37.9	<0.01
		Zn	84.9	<0.01
5	Back	Ca	91.2	<0.01
		Fe	93.8	<0.01
	Chest	Ca	129.0	<0.01
		Fe	25.6	<0.01
		Zn	75.6	<0.01
6	Chest	Ca	90.3	<0.01
		Fe	0.1	0.99
	Thigh	Ca	73.2	<0.01
		Fe	37.2	<0.01
		Zn	142.1	<0.01

Table 5.3: Elemental levels significance in the Epidermis compared to the dermis. Student's t-test and Wilcoxon test were used to identify p-values. 5-back and 6-chest were scanned with a 13 keV energy beam, thus Zn was not detected.

Table 5.3 shows that most elements are significantly present in the epidermis layer compared to the dermis (p-value <0.01). Only iron in 1-thigh (p-value = 0.50) and in 6-chest (p-value= 0.99) showed no significance. Here, pixel intensities were not sufficiently different, in either layer, to produce a visible difference in the map. Out of the three elements, Ca had the greatest % difference, between the two layers, with a range of 73.2% - 297.2% (mean of 140.1% and median of 109.1%), while Fe had the lowest % difference with a range of 7.4% - 113.3% (mean of 51.5% and median of 44.2%). Zn had a range of 33.0% - 268.6% (mean of 125.6% and median of 84.9%). This indicates that Ca had the clearest level distinction between the two layers, which is very evident from the maps in figure 5.4. Over all, it can be said with confidence that it is possible to clearly distinguish epidermis from the dermis in these maps using the μXRF technique.

The next step was to examine if any trends exist among the measured samples. Before making any comparisons, the significance of the difference in elemental levels between the same body parts from different cadavers was tested (e.g. testing if the Ca, Fe and Zn levels in all back samples are similar or significantly different from each other). It was found that the elemental levels between different cadavers were significant; thus, elemental intensities cannot be compared among different bodies (no medical records were provided for the cadavers, thus they cannot be treated as controls). Table 5.4 presents some comparisons among different sites, and elements.

Body #	Site	Decreasing order of elemental intensity in epidermis
1	Back	Ca > Fe> Zn
	Thigh	Zn> Ca*
2	Thigh	Ca > Fe> Zn
3	Back	Ca > Fe> Zn
	Chest	Ca > Fe> Zn
	Arm	Ca > Fe> Zn
4	Back	Ca > Fe> Zn
	Arm	Ca > Fe> Zn
	Thigh	Ca > Fe> Zn
5	Back	Fe> Ca**
	Chest	Fe> Zn> Ca
6	Thigh	Fe> Zn> Ca

* Fe eliminated because no significant difference was noted between the two layers
** was measured at 8 keV, so Zn was not detected.

Table 5.4: Possible trends between sites and elements

Table 5.4 shows that 8 out of 12 samples had the following elemental intensity trend: Ca > Fe> Zn (which was true for all samples from bodies 3 & 4 and all arm samples). 2 out of 4 thigh samples had higher Zn intensity compared to Ca. Other than the sample measured at 8 keV, all back samples followed the Ca > Fe> Zn trend.

All the data analysis shown above was obtained using 12 samples. The palm sample's analysis was conducted separately because 4 different regions of interest were taken into consideration rather than just two simple layers, as was shown before. Table 5.5 shows elemental levels significance among the different ROIs and their % difference.

a

Ca		**ROI 2**	**ROI 3**	**ROI 4**
	ROI 1	<0.01	0.276	<0.01
	ROI 2	---	<0.01	<0.01
	ROI 3	---	---	<0.01
Fe		**ROI 2**	**ROI 3**	**ROI 4**
	ROI 1	0.246	<0.01	0.206
	ROI 2	---	<0.01	<0.01
	ROI 3	---	---	<0.01
Zn		**ROI 2**	**ROI 3**	**ROI 4**
	ROI 1	<0.01	<0.01	<0.01
	ROI 2	---	<0.01	1.000
	ROI 3	---	---	<0.01

b

	ROI 2	**ROI 3**	**ROI 4**
ROI 1	106.2%	-6.6%	215.3%
ROI 2	---	-54.7%	52.9%
ROI 3	---	---	237.7%
	ROI 2	**ROI 3**	**ROI 4**
ROI 1	8.4%	-25.5%	-7.5%
ROI 2	---	-31.2%	-14.7%
ROI 3	---	---	24.1%
	ROI 2	**ROI 3**	**ROI 4**
ROI 1	89.3%	-37.8%	89.6%
ROI 2	---	-67.1%	0.2%
ROI 3	---	---	204.8%

Table 5.5: a: elemental levels significance among different ROIs and their b: % difference. ANOVA and Friedman tests were used to identify p-values

From table 5.5 (a), it can be seen that in general ROI 3 (spinosum/basale) has significant levels of all elements compared to other ROIs. The only exception is calcium's ROI 1 and ROI 3 because both regions have much higher peak intensities compared to the other 2 regions (at least 106% difference). For Zn, the highest % difference was between ROI 3 and ROI 4 (dermis) with a 204.8%. In the case of iron, the highest % difference was only 24.1% between ROI 3 and ROI 2.

Regarding skin tissues from different body parts, overall, most samples from the back gave the clearest distributions (only two are shown here, figure 5.4 d & e). The reason behind this could possibly be because the back has, overall, the thickest skin (the feet and palms have the thickest stratum corneum). Thicker skin means thicker individual

layers, thus more measured pixels at each layer. Other good sites for scanning were the thighs and the arms. The palms and feet have very thick stratum corneum. There are two disadvantages for scanning theses samples. The first one is much deeper scans have to be conducted, thus a lot more time is needed to finish one scan. The other reason is (this is specifically for the purpose of this study) that iron is found in the deepest part of the epidermis (a lot further away from the skin surface), thus feet and palms would not be ideal for in-vivo XRF iron measurements. Over all, chest samples did not show clear elemental distributions (especially for iron). Lastly, there was no clear site with the highest iron concentration, thus it cannot be concluded which site would give the best iron peak intensities.

Chapter 6: Conclusion & Future Work

In this thesis, a non-invasive method was investigated to determine an alternative solution to the invasive iron assessment in β-thalassemia patients. This method was in-vivo XRF iron measurements in skin. A calibration line was obtained using water phantoms and iron concentrations in the skin, liver and heart tissues of control mice were quantified. The range of iron concentrations in the mice skin was found to be -2 – 38 ppm and an average of 9.8 ± 1.6 ppm, which is in agreement with previous studies. A significant correlation (R^2 0.427) was found between iron levels in skin vs. heart. On the other hand, no significant correlation was found between the iron levels in skin vs. Liver (R^2 0.025). Human skin biopsies from 6 cadavers were collected and measured. The median of the iron concentration was found to be only 3 ppm, which is less than the average of 11 ppm reported in previous studies performed in living individuals.

Iron fluorescence's mean free path in water and soft tissues is 0.46 mm. Since skin is not a homogeneous tissue, it was important to investigate the distribution of iron in the skin using a synchrotron light facility. It was found that the presence of Ca, Fe, and Zn is significant in the epidermis layer compared to the dermis. In this study, it was hard to clearly distinguish the elemental distribution within the sub-layers of the epidermis. However, it was possible to identify the presence of Ca and Zn in the entire epidermal layer, whereas Fe was only found in the deeper region of epidermis. It was also

concluded that skin samples from the backs, arms and thighs are the best sites to be chosen for future studies.

For future work on XRF for β-thalassemia, measured tissues should be taken from iron-loaded mice rather than control mice. This would give a better understanding of the relationship of iron levels in the skin as a result of iron overload in β-thalassemic patients.

Based on the results from the synchrotron work, iron concentration in the skin should not be assumed to be homogeneous and phantoms should be constructed according to the fact that iron is concentrated at various depths from the surface.

Other XRF system could be built to obtain more accurate and precise measurements of trace-elements in general. A tri-axial XRF is one approach that is worth investigating. In this geometry, the x-ray tube, the secondary target and the sample are placed in a tri-axial geometry. "This allows a decrease in the background, using the advantages of the effect of polarization of the incident X-ray beam from the tube". [54, 55] With the use of appropriate collimators, the scattered radiation will be reduced, which will improve the detection limit. Also, while developing an XRF system, using a W-target x-ray tube would be a better option (compared to Mo-target) for iron studies. Using copper as a secondary target would be ideal because photons emitted from the copper target are very close to the K-absorption edge of iron (7.11 keV), thus iron fluorescence would be more efficient. Another approach would be to use a portable XRF system. Portable XRF machines are a much better option to use when considering in-vivo XRF

measurements in humans. It is worth investigating the MDL and trying to improve on what already exists.

Lastly, it was reported that when iron distribution was examined in patients with skin disorders, such as ulcers [27, 56] or the effect of ultra violet radiation [57], major iron deposition was found in the dermis layer rather than the epidermis. There are no studies addressing iron distribution across skin layers in β-thalassemic patients, which is worth investigating.

References

[1] Beard J L, Dawson H and Pinero D J, 1996. Iron Metabolism: A Comprehensive Review. *Nutr. Rev*. 54 (10): 295-317.

[2] Andrews N C, 1999. Disorders of Iron Metabolism. *N Engl. J. of Med.* 341 (26): 1986-1995.

[3] Pantopoulos K, 2004. Iron Metabolism and the IRE/IRP Regulatory System: An Update. *Ann. N.Y. Acad. Sci.* 1012: 1-13.

[4] Muncie H L and Campbell J C, 2009. Alpha and Beta Thalassemia. *Am. Fam. Phys.* 80 (4): 339-344.

[5] Mishra A K and Tiwari A, 2011. β-Thalassaemia - A Fatal Blood Disorder. *Int. J. Rev. Life Sci.* 1 (2): 83-87.

[6] Galanello R and Origa R, 2010. Beta-thalassemia. *Orphanet J. of Rare Diseases.* 5 (11): 1-15.

[7] Higgs D G, Engel J D and Stamatoyannopoulos G. Thalassaemia, 2012. *Lancet.* 379: 373-383.

[8] Rund D and Rachmilewitz E. β-Thalassemia, 2005. *N Engl. J. of Med.* 353 (11): 1135-1146.

[9] Farquharson M J and Bradley D A, 1999. The feasibility of a sensitive low-dose method for the in vivo evaluation of Fe in skin using K-shell x-ray fluorescence (XRF). *Phys. Med. Biol.* 44: 955-965.

[10] Knoll G F, 2000. *Radiation Detection and Measurement*, 3rd ed. New York: John Wiley &Sons Inc.

[11] Studinski R (2005). Development of an In Vivo Method of Measuring Arsenic with Radiation. Unpublished Doctor of Philosophy Thesis, McMaster University, Hamilton, ON, Canada.

[12] Carew S (2001). The Use of In Vivo X-Ray Fluorescence Measurements in the Analysis of Cadmium Toxicology. Unpublished Master's Thesis, McMaster University, Hamilton, ON, Canada.

[13] Lawrence Berkeley National Laboratory (LBL), Fluorescence and Coster-Kronig Yields. Retrieved March 10, 2012, from: http://ie.lbl.gov/atomic/flo.pdf

[14] Lawrence Berkeley National Laboratory (LBL), X-Ray Data Book. Retrieved October 23, 2011, from: http://xdb.lbl.gov/xdb-new.pdf

[15] X-ray Fluorescence. [Image online]. Retrieved October 23, 2011, from: http://projects.exeter.ac.uk/geomincentre/estuary/Main/fluorescence.htm

[16] Gartner L P and Hiatt J L, 2011. *Concise Histology.* Philadelphia: Saunders Elsevier.

[17] Eroschenko V P, 2005. *diFiore's Atlas of Histology with Functional Correlations,* 10th ed. Philadelphia: Lippincott Williams & Wilkins.

[18] Skin Layers. A.D.A.M., Inc. University of Maryland Medical Center (UMMC). [Image online]. Retrieved March 13, 2012, from: http://www.umm.edu/imagepages/8912.htm

[19] Epidermis (Skin). [Image online]. Retrieved July 25, 2012, from: http://en.wikipedia.org/wiki/Epidermis_%28skin%29

[20] Valentin J, 2002. Basic Anatomical and Physiological Data for Use in Radiological Protection: Reference Values: ICRP Publication 89. *Annals of the ICRP.* 32 (3-4): 1-277.

[21] Papassotirious V, Georgala S, Stratigos J, Panayotakis N, Hadjiantoniou A and Katsanos A A, 1986. Trace Elements in Skin Epitheliomas. *J. of Radioanal. Nucl. Chem.* 109 (1): 89-100.

[22] Gorodetsky R, Goldfarb A, Dangan I and Rachmilewitz E A, 1985. Noninvasive analysis of skin iron and zinc levels in β-thalassemia major and intermedia. *J. Lab. Clin. Med.* 105 (1): 44-51.

[23] Gorodetsky R, Sheskin J and Weinreb A, 1986. Iron, Copper, and Zinc Concentrations in Normal Skin and in Various Nonmalignant and Malignant Lesions. *Intl. J. of Dermatology.* 25 (7): 440-445.

[24] Gorodetsky R, Loewenthal E, Goldfarb A and Rachmilewitz E A, 1990. Non-Invasive Evaluation of Iron Load and Clearance in Patients with β-Thalassemia. *Ann. NY Acad. Sci.* 612 (1): 568-572.

[25] Farquharson M J, Bagshaw AP, Porter J B and Abeysinghe R D, 2000. The use of skin Fe levels as a surrogate marker for organ Fe levels, to monitor treatment in cases of iron overload. *Phys. Med. Biol.* 45: 1-10.

[26] Bagshaw A P and Farquharson M J, 2001. Simultaneous determination of iron, copper and zinc concentrations in skin phantoms using XRF spectrometry. *X-Ray Spectrom*. 31: 47-52.

[27] Ackerman Z, Seidenbaum M, Loewenthal E and Rubinow A, 1988. Overload of Iron in the Skin of Patients with Varicose Ulcers: Possible Contributing Role of Iron Accumulation in Progression of the Disease. *Archives of Dermatology.* 124: 1376-1378.

[28] Marcelo E and Appoloni C R, 2009. Use of portable X-ray fluorescence (XRF) in vivo as an alternative technique for monitoring of iron levels in patients with iron overload. *Rev. Bras. Hematol. Hemoter.* 31 (3): 153-159.

[29] Pakbaz Z, Fischer R, Fung E, Nielsen P, Harmatz P and Vichinsky E, 2007. Serum Ferritin Underestimates Liver Iron Concentration in Transfusion Independent Thalassemia Patients as Compared to Regularly Transfused Thalassemia and Sickle Cell Patients. *Padiatr. Blood Cancer.* 49 (3): 329-332.

[30] Molin L and Wester P O, 1976. The Estimated Daily Loss of Trace Elements from Normal Skin by Desquamation. *Scand. J. clin. Lab. Invest.* 36: 679-682.

[31] Parr R M and Taylor D M, 1964. The Concentrations of Cobalt, Copper, Iron and Zinc in some Normal Human Tissues as Determined by Neutron- Activation Analysis. *Biochem. J.* 91: 424-431.

[32] Milstone L M, Hu R, Dziura J D and Zhou J, 2012. Impact of epidermal desquamation on tissue stores of iron. *J. Dermatol. Sci.* 67: 9-14.

[33] Torrance J D and Bothwell T H, 1980. *Tissue iron.* In: *Methods in Hematology*, vol. 1. New York: Churchill Livingston Press.

[34] Waittaker P, Hines F A, Robl M G and Dunkel V C, 1996. Histopathological Evaluation of Liver, Pancreas, Spleen, and Heart from Iron-Overloaded Sprague-Dawley Rats. *Toxicol. Pathol.* 24 (5): 558-563.

[35] Yue GZ, Qiu Q, Gao B, Cheng Y, Zhang J, Shimoda H, Chang S, Lu J P and Zhou O, 2002. Generation of continuous and pulsed diagnostic imaging x-ray radiation using a carbon-nanotube-based field-emission cathode. *Appl. Phys. Lett.* 81 (2): 355-357.

[36] Dhillon V. The Atmoshphere, 2010. [Image online]. Retrieved July 03, 2012, from: http://www.vikdhillon.staff.shef.ac.uk/teaching/phy217/telescopes/phy217_tel_atmos.html

[37] Schultz M K, Keyser R M, Trammell R C and Upp D L, 2007. Improvement of spectral resolution in the presence of periodic noise and microphonics for hyper-pure germanium detector gamma-ray spectrometry using a new digital filter. *J. Rad. Nucl. Chem.*271 (1): 101 – 106.

[38] "Interference". 2012. In *oxforddictionaries.com*. Retrieved July 17, 2012, from http://oxforddictionaries.com/definition/english/interference?q=interference

[39] M. K. Sue. Radio Frequency Interference at the Geostationary Orbit. Final Report. *NASA. Jet Propulsion Laboratory*. 1981. Retrieved July 17, 2012, from http://ntrs.nasa.gov/archive/nasa/casi.ntrs.nasa.gov/19810018807_1981018807.pdf

[40] Carl Salter, 2009. Error Analysis Using the Variance-Covariance Matrix. *J Chem. Edu.* 77 (9): 1239 – 1243.

[41] In collaboration with Elstan Desouza, PhD candidate, McMaster University. 2012

[42] Adams B D, Lazova R, Andrews N C and Milstone L M, 2005. Iron in Skin of Mice with Three Etiologies of Systemic Iron Overload. *J. Invest. Dermatol.* 125: 1200-1205.

[43] Molin L and Wester P O, 1973. Iron content in normal and psoriatic epidermis. *Acta Derm Venereol (Stockh).* 53: 473-476.

[44] Malmqvist K G, Carlsson L E, Forslind B, Roomans G M and Akselsson K R, 1984. Proton and Electron Microprobe Analysis of Human Skin. *Nucl. Instrum. Methods Phys. Res.* B3: 611-617.

[45] Malmqvist K G, Forslind B, Themner K, Hylten G, Grundin T and Roomans G M, 1987. The use of PIXE in Experimental Studies of the Physiology of Human Skin Epidermis. *Biol. Trace Elem. Res.* 12: 297-308.

[46] Werner-Linde Y, Pallo J and Forslin B. Physiologically Important Trace Elements of Paralesional Psoriatic Skin, 1998. *Scanning Microscopy*. 12 (4): 599-608.

[47] Forslin B, Werner-Linde Y, Lindberg M and Pallon J, 1999. Elemental Analysis Mirrors Epidermal Differentiation. *Acta Derm Venereol (Stockh).* 79: 12-17.

[48] Forslin B, 2000. The skin barrier: analysis of physiologically important elements and trace elements. *Acta Derm Venereol (Stockh).* Supp 208: 46-52.

[49] How does the CLS synchrotron work? *Canadian Light Source.* Retrieved July 30, 2012, from http://www.lightsource.ca/education/pdf/materials/1.2_How_does_the_CLS_Synchrotron_work.pdf

[50] Margaritondo G, 2002. *Elements of Synchrotron Light: For Biology, Chemistry, and Medical Research*. New York: Oxford University Press.

[51] National Synchrotron Light Source, 2007. *Brookhaven National Laboratory*: Upton, NY. Retrieved July 30, 2012 from http://www.bnl.gov/bnlweb/pubaf/fact_sheet/pdf/trifold_NSLS.pdf

[52] About VESPERS, 2009. *University of Western Ontario and the Canadian Light Source*. Retrieved July 30, 2012, from http://www.vespersbeamline.com/about.php

[53] Feng R, 2007. Very Sensitive Elemental and Structural Probe Employing Radiation from a Synchrotron (VESPERS) Beamline 07B2-1. *Canadian Light Source Activity Report*: 166-168.

[54] Gonzalez-Fernandez O, Queralt I, Carvalho M L and Garcia G, 2007. Elemental analysis of mining wastes by energy dispersive X-ray fluorescence (EDXRF). *Nucl. Instrum. Methods Phys. Res.* B 262: 81-86.

[55] Gonzalez-Fernandez O, Pessanha S, Queralt I and Carvalho M L, 2009. Analysis of lead content in automotive shredder residue (ASR). *Waste Manage.* 29: 2549-2552.

[56] Caggiati A, Rosi C, Casini A, Cirenza M, Petrozza V, Acconcia M C and Zamboni P, 2010. Skin Iron Deposition Characterises Lipodermatosclerosis and Leg Ulcer. *Eur. J. Vasc. Endovasc. Surg.* 40: 777-782.

[57] Bissett D L, Chatterjee R and Hannon D P, 1991. Chronic Ultra Violet Tadiation-Induced Increase in Skin Iron and the Photoprotective Effect of Topically Applied Iron Chelators. *Photochem. Photobiol.* 54 (2): 215-233.